

## Long-lived NLSP in the NMSSM

Amit Adhikary<sup>1,\*</sup>, Rahoo Kumar Barman<sup>2,†</sup>, Biplob Bhattacharjee<sup>3,‡</sup>, Amandip De<sup>3,§</sup>,  
Rohini M. Godbole<sup>3,||</sup> and Suchita Kulkarni<sup>4,¶</sup>

<sup>1</sup>*Institute of Theoretical Physics, Faculty of Physics, University of Warsaw,  
Pasteura 5, PL 02-093, Warsaw, Poland*

<sup>2</sup>*Department of Physical Sciences, Oklahoma State University, Stillwater, Oklahoma 74078, USA*

<sup>3</sup>*Centre for High Energy Physics, Indian Institute of Science, Bengaluru 560012, India*

<sup>4</sup>*Institute of Physics, NAWI Graz, University of Graz, Universitätsplatz 5, A-8010 Graz, Austria*



(Received 16 July 2022; accepted 24 July 2023; published 16 August 2023)

We analyze the scenario within the next to minimal supersymmetric Standard Model, where the lightest supersymmetric particle is singlinolike neutralino. By systematically considering various possible admixtures in the electroweakino sector, we classify regions of parameter space where the next to lightest supersymmetric particle is a long-lived electroweakino while remaining consistent with constraints from flavor physics, dark matter direct detection, and collider data. We identify viable cascade decay modes featuring the long-lived next to lightest supersymmetric particle for directly produced chargino-neutralino pairs, thus, leading to displaced vertex signatures at the high luminosity LHC (HL-LHC). We construct a track-based analysis in order to uncover such scenarios at the HL-LHC and analyze their discovery potential. We show that through such focused searches for the long-lived particles at the HL-LHC, one can probe regions of the electroweakino parameter space that are otherwise challenging.

DOI: [10.1103/PhysRevD.108.035020](https://doi.org/10.1103/PhysRevD.108.035020)

### I. INTRODUCTION

Observations of the existence and measurements of dark matter (DM) [1,2], of matter-antimatter asymmetry and nonzero neutrino masses [2], as well as theoretical considerations such as the hierarchy problem [3–5] point to the existence of new physics beyond that in the Standard Model (SM). Among the extensions of the SM, those involving supersymmetry (SUSY) still remain one of the most appealing because they address multiple shortcomings of the SM at once [6–10]. Depending on the exact realization, SUSY can present numerous DM candidates such as the lightest neutralino, sneutrino, or gravitino [9,11–13]. The SUSY DM candidate, viz. the lightest supersymmetric particle (LSP), is stabilized by means of an external symmetry, such as  $R$  parity; see, for example, [9,10].

The interactions of the DM with the particles in the SM or those within the dark sector affect its exact evolution and hence subsequently, the prediction for the amount remaining today, dubbed as relic density. This has been now accurately measured to be  $\Omega h^2 = 0.120 \pm 0.001$  [1] where  $h$  is Hubble constant in units of  $100 \text{ km s}^{-1} \text{ Mpc}^{-1}$ . In case of the neutralino LSP, the relic density is often generated utilizing the popular thermal freeze-out process [14–16], while for gravitino, the suppressed couplings with the SM necessitate a nonthermal relic density generation mechanism [17,18]. Apart from the particle physics aspect, the relic density also depends on the details of the early Universe evolution. For example, late-time entropy production can substantially dilute the relic density while keeping the particle physics details unchanged. In the absence of precise knowledge of DM interactions and the evolution of the early Universe, it is thus important to consider both overabundant and underabundant [viz. witch predicted relic density has a value above (below) the measured value] regions of SUSY DM parameter space [13,19–24].

Dark matter can be searched for in several experiments. Due to model-independent search strategies, the results are applicable to SUSY and a variety of other beyond the SM scenarios. The primary detection strategies are via detection of missing energy at the LHC, via scattering off nuclei at underground direct detection experiments, or via detection of decay or annihilation products through cosmic rays in

\*amit.adhikary@fuw.edu.pl

†rahoor.barman@okstate.edu

‡biplob@iisc.ac.in

§amandipde@iisc.ac.in

||rohini@iisc.ac.in

¶suchita.kulkarni@uni-graz.at

Published by the American Physical Society under the terms of the [Creative Commons Attribution 4.0 International license](https://creativecommons.org/licenses/by/4.0/). Further distribution of this work must maintain attribution to the author(s) and the published article's title, journal citation, and DOI. Funded by SCOAP<sup>3</sup>.

the Universe today at indirect detection experiments. Among these, the direct detection experiments already rule out left-handed sneutrino DM arising in the minimal supersymmetric Standard Model [25]. Out of the thermal candidates, this leaves the lightest neutralino—a linear combination of the bino, wino, and Higgsino—as a viable DM candidate, whose compatibility with the experimental searches needs to be checked in detail.

In the minimal supersymmetric Standard Model (MSSM), the lightest neutralino is a part of the system of electroweakinos, which consists of four neutralinos and two charginos. The electroweakino sector, and in particular, light neutralinos, have been a topic of intense phenomenological and experimental investigations in the past decade. Some of the latest LHC results for electroweakino searches are summarized below. A CMS search for electroweakinos through chargino-neutralino production ( $\tilde{\chi}_1^\pm \tilde{\chi}_2^0$ ) with on-shell decays to  $Wh$  final state rules out winolike chargino masses up to 700 GeV, for binolike LSP mass  $M_{\tilde{\chi}_1^0} < 350$  GeV [26]. This search was performed at the center-of-mass energy of 13 TeV with an integrated luminosity of  $137 \text{ fb}^{-1}$ . Another search from the ATLAS collaboration considers pair production of neutralinos at 13 TeV with  $139 \text{ fb}^{-1}$  integrated luminosity in fully hadronic final states mediated by  $WW, WZ$ , or  $Zh$  [27]. This search excludes wino (Higgsino) mass up to 1060 (900) GeV for binolike LSP up to 400 (200) GeV. These searches imply a relatively heavier electroweakino sector. It should, however, be noted that these results assume a simplified model framework with 100% branching ratios, which should be reinterpreted in the context of specific SUSY models, e.g., phenomenological MSSM or next-to-MSSM (NMSSM). As a result, lighter electroweakinos can still be allowed despite the stringent LHC limits, and the exact limits are model dependent.

Some generic conclusions about the MSSM neutralino dark matter in light of recent collider and astrophysical constraints are available now. For example, the neutralino masses in phenomenological MSSM have a lower limit of  $M_{\tilde{\chi}_1^0} > 34$  GeV in order to avoid overabundant relic density [24,28–31]. In the general-MSSM scenario, Higgsinos are favored to have mass  $\sim 1$  TeV to obtain the correct DM abundance for a single component thermal DM [32–34]. Within the MSSM, relic density compliant regions require either heavy DM or rely on a coannihilation mechanism, which demands a small mass splitting between DM and its coannihilating partner. Such small mass gaps can lead to long-lived particles (LLPs), which can then be investigated, for example, by looking for displaced vertices or heavy stable charged particles. It is worth noting that relaxing the DM relic density requirement does not necessarily lead to additional LLP parameter space within the MSSM. This is because the only way to obtain LLPs is through small mass splitting, as the SUSY couplings are related to those of SM and hence cannot be suppressed.

Although the MSSM can successfully provide a DM candidate, a drawback of this most commonly used SUSY realization is the “ $\mu$  problem” which arises as an artifact of the common mass term for two Higgs doublets. This introduces a fine-tuning, which requires an electroweak scale  $\mu$  parameter rather than the expected Planck scale [35]. An alternative can be considered as a singlet extension of the MSSM, the NMSSM [36–38] with a singlet Higgs field in addition to two Higgs doublets of the MSSM. For this additional scalar, the effective  $\mu$  term can be generated dynamically, alleviating the fine-tuning of  $\mu$ . The fermionic component of the singlet superfield provides an additional neutralino without violating the existing constraints. In such cases, the LSP can be pure singlino dominated or a mixture of Higgsino-singlino. Such LSP can be lighter than the corresponding MSSM counterpart [39–43].

The phenomenology of such extended sectors can open up interesting new avenues for DM phenomenology as well as experimental searches. In this work, we revisit the neutralino sector of the NMSSM, focusing on the LSP with a significant singlino fraction [44–47]. Such singlino has suppressed couplings with the rest of the SUSY spectrum and thus can lead to a long-lived NLSP neutralino. We investigate this possibility and suggest a displaced vertex search relying on tracks originating through NLSP decays. It should be noted that the region of the LLP parameter space in the NMSSM considered in this work has two distinct features. First, the long-lifetime of the NLSP neutralino results from suppressed couplings and small mass differences with the singlino-dominated LSP neutralino, and second, it leads to overabundant relic density for the LSP neutralino DM.

The LLPs are intriguing since they lead to characteristic collider signatures. The charge and color-neutral LLPs travel a macroscopic distance before decaying into SM particles at a secondary vertex, resulting in a displaced vertex signature. The LLPs can be realized either with scenarios involving suppressed couplings or small mass splittings. Depending on the LLP lifetime, its decay may take place either in the tracker, in calorimeters and muon system, or even outside the detector. The pivotal advantage is having an almost negligible background, thanks to the existence of displaced vertices. A variety of theory scenarios, including SUSY, little Higgs [48], twin Higgs [49], dark sector models [50–54] etc., predict LLPs. In SUSY, LLPs are usually featured in  $R$ -parity violating models [55]. Besides, in many  $R$ -parity conserving scenarios gauge-mediated SUSY [56,57], anomaly-mediated SUSY [58], particles with long lifetime can appear.

The long-lived NLSP neutralino within the NMSSM is thus an exciting prospect, and a potential discovery could lead to a renewed understanding of the behavior of dark matter in the early Universe. We, therefore, present a

detailed search strategy for such parameter space in this work. The rest of the paper is organized as follows. In Sec. II, we briefly review the NMSSM framework and motivation for the relevant parameters to single out the region of interest. Section III describes the pertinent range of parameters for numerical scan, along with the current phenomenological constraints. The characteristic features of the parameters to achieve long-lived neutralinos are discussed in Sec. IV. In Sec. V we present a signal-to-background study via searches of displaced vertices from decays of long-lived neutralinos and explore the reach of such searches for direct production of electroweakinos at the high luminosity LHC (HL-LHC). Finally, we conclude in Sec. VI.

## II. THE NMSSM FRAMEWORK

### A. Higgs sector

In this section, we discuss the Higgs and electroweakino sectors in the NMSSM. The NMSSM Higgs sector consists of a singlet superfield  $\hat{S}$  and two doublet Higgs superfields,  $\hat{H}_u$  and  $\hat{H}_d$ . The dimensionful couplings of  $\hat{S}$  can be forbidden through a discrete  $\mathcal{Z}_3$  symmetry leading to scale-invariant NMSSM superpotential [59]

$$W_{\text{NMSSM}} = W_{\text{MSSM}}(\mu = 0) + \lambda \hat{S} \hat{H}_u \cdot \hat{H}_d + \frac{1}{3} \kappa \hat{S}^3. \quad (2.1)$$

Here,  $W_{\text{MSSM}}(\mu = 0)$  is the MSSM superpotential without the  $\mu$  term, while  $\lambda$  and  $\kappa$  are dimensionless couplings. The  $\lambda \hat{S} \hat{H}_u \cdot \hat{H}_d$  term generates an effective MSSM-like  $\mu$  term when  $\hat{S}$  develops a vacuum expectation value  $v_s$ ,  $\mu = \lambda v_s$ . Thus, the  $\mu$  term in NMSSM is generated ‘‘dynamically,’’ providing a solution to the MSSM  $\mu$  problem [35] when  $v_s$  is at the electroweak scale [60]. The soft SUSY breaking terms containing the singlet and doublet Higgs fields have the form

$$V_{\text{soft}} = m_{H_u}^2 |H_u|^2 + m_{H_d}^2 |H_d|^2 + m_S^2 |S|^2 + \left( \lambda A_\lambda S H_u \cdot H_d + \frac{1}{3} \kappa A_\kappa S^3 + \text{H.c.} \right), \quad (2.2)$$

where  $m_{H_u}$ ,  $m_{H_d}$ ,  $m_S$  are the soft breaking Higgs masses, and  $A_\lambda$ ,  $A_\kappa$  are the trilinear couplings. The Higgs scalar potential  $V$  is also augmented by  $F$  and  $D$  terms,

$$V_F = |\lambda H_u \cdot H_d + \kappa S^2|^2 + \lambda^2 |S|^2 (H_u^\dagger H_u + H_d^\dagger H_d), \\ V_D = \frac{g_1^2 + g_2^2}{8} (H_u^\dagger H_u - H_d^\dagger H_d)^2 + \frac{g_2^2}{2} |H_d^\dagger H_u|^2, \quad (2.3)$$

respectively. In Eq. (2.3)  $g_1$  and  $g_2$  are the SM  $U(1)_Y$  and  $SU(2)_L$  gauge couplings, respectively. The physical Higgs states  $\{H_u^0, H_d^0, S\}$  can be obtained by expanding the Higgs scalar potential in Eqs (2.2) and (2.3),  $V_{\text{soft}} + V_D + V_F$ ,

around real neutral vacuum expectation values  $v_u$ ,  $v_d$ , and  $v_s$ , and following the notation of [61], are given by

$$H_u^0 = \frac{v_u + H_u^R + iH_u^I}{\sqrt{2}}, \\ H_d^0 = \frac{v_d + H_d^R + iH_d^I}{\sqrt{2}}, \quad S = \frac{v_s + H^S + iA^S}{\sqrt{2}}. \quad (2.4)$$

Here,  $\{H_u^R, H_d^R, H^S\}$  are the real components while  $\{H_u^I, H_d^I, A^S\}$  are the imaginary components. The three real components lead to three neutral  $CP$ -even Higgs bosons. One neutral pseudoscalar Higgs boson stems from the imaginary components  $\{H_u^I, H_d^I\}$ , while  $\{A^S\}$  leads to another neutral pseudoscalar Higgs boson. The mass matrix elements of  $CP$ -even Higgs can be computed in a rotated  $CP$ -even Higgs interaction basis  $\{H^{\text{SM}}, H^{\text{NSM}}, H^S\}$  where  $H^{\text{SM}}$ ,  $H^{\text{NSM}}$ , and  $H^S$  corresponds to SM-like, MSSM-like heavy Higgs, and singlet scalar Higgs eigenstates, respectively. The elements of the  $3 \times 3$  symmetric mass-squared matrix  $M_S^2$  in this basis are given by [60–62]

$$M_{S,11}^2 = \left( m_Z^2 - \frac{1}{2} \lambda^2 \right) \sin 2\beta^2 + \frac{\mu}{\sin \beta \cos \beta} \left( A_\lambda + \frac{\kappa \mu}{\lambda} \right), \\ M_{S,22}^2 = m_Z^2 \cos 2\beta^2 + \frac{1}{2} \lambda^2 v^2 \sin 2\beta^2, \\ M_{S,33}^2 = \frac{1}{4} \lambda^2 v^2 \sin 2\beta \left( \frac{A_\lambda}{\mu} \right) + \frac{\kappa \mu}{\lambda} \left( A_\kappa + \frac{4\kappa \mu}{\lambda} \right), \\ M_{S,12}^2 = \left( \frac{1}{2} \lambda^2 v^2 - m_Z^2 \right) \sin 2\beta \cos 2\beta, \\ M_{S,13}^2 = -\frac{1}{\sqrt{2}} \lambda v \cos 2\beta \left( \frac{2\kappa \mu}{\lambda} + A_\lambda \right), \\ M_{S,23}^2 = \sqrt{2} \lambda v \mu \left( 1 - \frac{A_\lambda}{2\mu} \sin 2\beta - \frac{\kappa}{\lambda} \sin 2\beta \right). \quad (2.5)$$

Here,  $\beta = \tan^{-1} \frac{v_u}{v_d}$  with  $\sqrt{v_u^2 + v_d^2} = v \simeq 246$  GeV and  $m_Z$  represents the  $Z$  boson mass. The  $CP$ -even Higgs mass eigenstates  $H_i$  ( $i = 1, 2, 3$ ) can be obtained by diagonalizing  $M_S^2$  through an orthogonal rotation matrix  $V$ ;  $H_i = \sum_{j=1}^3 V_{i,j} \phi_{jR}$ , where  $\phi_R = \{H^{\text{SM}}, H^{\text{NSM}}, H^S\}$ , and  $m_{H_1} < m_{H_2} < m_{H_3}$ . In the present study, we require  $H_1$  to be consistent with the properties of the observed 125 GeV Higgs boson. Introducing

$$M_\lambda^2 = \frac{\mu}{\sin \beta \cos \beta} \left( A_\lambda + \frac{\kappa \mu}{\lambda} \right) \quad (2.6)$$

the elements of the  $2 \times 2$  symmetric mass-squared matrix  $M_P^2$  after dropping the Goldstone modes in the pseudoscalar Higgs interaction basis  $\phi_I = \{A^{\text{NSM}}, A^S\}$  can be written as

$$\begin{aligned}
 M_{P,11}^2 &= M_A^2, \\
 M_{P,22}^2 &= \frac{1}{2} \lambda^2 v^2 \sin 2\beta \left( \frac{M_A^2}{4\mu^2} \sin 2\beta + \frac{3\kappa}{2\lambda} \right) - \frac{3\kappa A_\kappa \mu}{\lambda}, \\
 M_{P,12}^2 &= -\frac{1}{\sqrt{2}} \lambda v \left( \frac{3\kappa\mu}{\lambda} - \frac{M_A^2}{2\mu} \sin 2\beta \right). \tag{2.7}
 \end{aligned}$$

Here again, following a similar recipe, the  $CP$ -odd Higgs mass eigenstates  $\{A_m = A_1, A_2\}$  ( $m_{A_1} < m_{A_2}$ ) can be written as  $A_m = \sum_{n=1}^2 P_{m,n} \phi_{nI}$ , where  $m = 1, 2$  and  $P_{m,n}$  is an orthogonal rotation matrix.

In addition to the three  $CP$ -even and the two  $CP$ -odd neutral Higgs states, the NMSSM framework also predicts a pair of charged Higgs bosons  $H^\pm$ . At the tree level, their masses are given by

$$M_{H^\pm}^2 = M_A^2 + m_W^2 - \frac{1}{2} \lambda^2 v^2, \tag{2.8}$$

where  $m_W$  is the mass of the  $W$  boson. Overall, the tree-level Higgs sector of NMSSM can be parametrized by the following six parameters:

$$\lambda, \kappa, A_\lambda, A_\kappa, \tan \beta, \mu \tag{2.9}$$

## B. Electroweakino sector

The NMSSM electroweakino sector consists of bino  $\tilde{B}^0$ , neutral wino  $\tilde{W}_3^0$ , Higgsinos  $\tilde{H}_d^0, \tilde{H}_u^0$ , and singlino  $\tilde{S}$  leading to five neutralinos, and two chargino mass eigenstates from admixture of charged wino and charged Higgsinos. In the  $\{\tilde{B}, \tilde{W}_3^0, \tilde{H}_d^0, \tilde{H}_u^0, \tilde{S}\}$  basis, the symmetric  $5 \times 5$  neutralino mass matrix  $M_{\tilde{N}}$  can be written as

$$M_{\tilde{N}} = \begin{pmatrix} M_1 & 0 & -m_Z \sin \theta_W \cos \beta & m_Z \sin \theta_W \sin \beta & 0 \\ 0 & M_2 & m_Z \cos \theta_W \cos \beta & -m_Z \cos \theta_W \sin \beta & 0 \\ -m_Z \sin \theta_W \cos \beta & m_Z \cos \theta_W \cos \beta & 0 & -\mu & -\lambda v \sin \beta \\ m_Z \sin \theta_W \sin \beta & -m_Z \cos \theta_W \sin \beta & -\mu & 0 & -\lambda v \cos \beta \\ 0 & 0 & -\lambda v \sin \beta & -\lambda v \cos \beta & 2\kappa v_s \end{pmatrix}. \tag{2.10}$$

Here,  $M_1$  is the bino mass parameter,  $M_2$  is the wino mass parameter, and  $\theta_W$  is the Weinberg angle. Diagonalizing  $M_{\tilde{N}}$  through an  $5 \times 5$  orthogonal rotation matrix  $\hat{N}$  leads to the neutralino mass eigenstates  $\tilde{\chi}_i^0$ ,

$$\tilde{\chi}_i^0 = \hat{N}_{i1} \tilde{B}^0 + \hat{N}_{i2} \tilde{W}_3^0 + \hat{N}_{i3} \tilde{H}_d^0 + \hat{N}_{i4} \tilde{H}_u^0 + \hat{N}_{i5} \tilde{S}. \tag{2.11}$$

Similarly, the charged winos and Higgsinos mix to generate the two charginos  $\tilde{\chi}_i^\pm$  ( $i = 1, 2$ ). The input parameters that regulate the electroweakino sector at the tree level are as follows:

$$M_1, M_2, \mu, \tan \beta, \lambda, \kappa. \tag{2.12}$$

The lightest neutralino  $\tilde{\chi}_1^0$  naturally provides a DM candidate in  $R$ -parity conserving NMSSM. *A priori*, the LSP  $\tilde{\chi}_1^0$  can be pure gaugino, Higgsino, singlino, or an admixture of these states. Such an LSP can lead to the correct DM relic density either if it is purely Higgsino or winolike with masses up to 2.8 TeV [63,64] or if it is bino- or singlinolike, which can annihilate through coannihilation or resonant annihilation through Higgs or  $Z$  boson. Such resonant annihilation conditions can only be realized for  $m_{\tilde{\chi}_1^0} \sim m_{H/Z}/2$ , subject to non-negligible  $\tilde{\chi}_1^0 \tilde{\chi}_1^0 Z/H$  couplings. In this work, however, we do not impose any relic density requirements and the allowed parameter space points of our interest are all overabundant. For these scenarios, the relic density can be fulfilled either by

requiring additional DM candidates or by requiring non-standard evolution of the Universe, as argued in Sec. I.

## III. PARAMETER SPACE SCAN AND CONSTRAINTS

Our primary focus is the region in the parameter space of the  $R$ -parity conserving NMSSM, featuring a long-lived neutralino while being consistent with the current collider and direct/indirect detection constraints. To this end, we consider a dominantly singlinolike LSP  $\tilde{\chi}_1^0$  and binolike NLSP  $\tilde{\chi}_2^0$ . Since there are no tree-level couplings between the bino and singlino, the binolike NLSP  $\tilde{\chi}_2^0$  decays to the singlinolike LSP  $\tilde{\chi}_1^0$  only through their mutual Higgsino admixtures. This leads to a suppressed coupling between LSP and NLSP states. An additional phase space suppression can be achieved if the mass difference between the two states is smaller than the  $Z$  mass. In such scenarios, the binolike  $\tilde{\chi}_2^0$  can be LLP. The heavier neutralinos  $\tilde{\chi}_3^0, \tilde{\chi}_4^0, \tilde{\chi}_5^0$ , and charginos  $\tilde{\chi}_1^\pm, \tilde{\chi}_2^\pm$  can be either Higgsinolike, winolike, or admixtures of both and decay promptly. In this analysis, we consider a moderately mixed scenario with  $\mu < M_2$ , which implies a relatively large Higgsino admixture in  $\tilde{\chi}_3^0, \tilde{\chi}_4^0$ , and  $\tilde{\chi}_1^\pm$ .

Our choice for  $\mu < M_2$  is motivated by three factors. First, LHC constraints for Higgsinos are weaker compared to winos [26,27]. Second, Higgsinos have tree-level couplings with both singlino and bino, while no such interactions exist for wino-bino or wino-singlino instances.

Therefore, winos can decay into bino or singlino only by virtue of its mixing with Higgsinos. Third, both binolike  $\tilde{\chi}_2^0$  and singlinolike  $\tilde{\chi}_1^0$  are required to have nonzero Higgsino admixtures in order to generate a tractable decay width for  $\tilde{\chi}_2^0$  such that they can be probed at the LHC through track-based LLP searches. Concretely, we choose  $500 \text{ GeV} \lesssim \mu \lesssim 1000 \text{ GeV}$ ,  $M_2 \geq 2 \text{ TeV}$  such that  $\tilde{\chi}_3^0, \tilde{\chi}_4^0$ , and  $\tilde{\chi}_1^\pm$  have a dominant Higgsino admixture with appreciable production rates at HL-LHC, compatible with existing LHC constraints from direct electroweakino searches, discussed in Sec. III B.

In the NMSSM superpotential as given in Eq. (2.1), we observe that interactions between the singlet superfield  $\hat{S}$  and the MSSM Higgs superfields  $\hat{H}_u, \hat{H}_d$  is controlled by  $\lambda$ . In the limit,  $\lambda \rightarrow 0$  (for a fixed  $\mu = \lambda v_S$ ), the singletlike scalar, singletlike pseudoscalar, and the singlino can no longer interact with the MSSM sector. This consideration leads to the possibility of a pure singlinolike neutralino LSP with a tree level mass  $\sim 2\kappa v_S$ . In this case, the NLSPs would be composed of bino/wino/Higgsinos, similar to that in MSSM. Furthermore, in the  $\lambda \rightarrow 0$  limit, the LSP has no interaction with NLSPs, however, keeping a finite but small  $\lambda$  leads to suppressed interactions between singlino LSP and MSSM-like neutralino NLSPs. This suppression leads to long-lived NLSPs, which is the focus of this work. In particular, we consider binolike  $\tilde{\chi}_2^0$ . In the limit,  $\mu \gg 2\kappa v_S$ , the mass of the singlinolike neutralino  $m_{\tilde{\chi}_1^0}$  can be approximated as

$$m_{\tilde{\chi}_1^0} \sim 2\kappa v_S \simeq 2 \frac{\kappa}{\lambda} \mu. \quad (3.1)$$

We, therefore, observe that a singlinolike LSP with a typical mass of  $\mathcal{O}(100) \text{ GeV}$  and  $\mu \sim \mathcal{O}(500) \text{ GeV}$  leads to  $\kappa/\lambda \sim \mathcal{O}(0.1)$ . In order to maintain a similar mass hierarchy between the Higgsinolike neutralinos and the singlinolike  $\tilde{\chi}_1^0$ , we restrict ourselves to  $\kappa/\lambda \leq 0.15$  with  $10^{-5} \leq \lambda \leq 10^{-1}$ . Correspondingly, for the sake of simplicity, we restrict ourselves to the parameter space where singlinolike LSP mass is  $\mathcal{O}(100) \text{ GeV}$ . We are thus left with the bino mass parameter,  $M_1$ , the only remaining parameter in the electroweakino mass spectrum, which is not fixed. Since we are interested in a binolike  $\tilde{\chi}_2^0$ , it must fall between the singlino- and Higgsinolike neutralinos. Correspondingly, we vary  $M_1$  over the range  $150 \text{ GeV} \leq M_1 \leq 550 \text{ GeV}$ . We illustrate the mass hierarchy between the electroweakinos in Fig. 1. The other input parameters that are relevant to the present study are  $A_\lambda, A_\kappa$ , the gluino mass parameter  $M_3$ , squark mass parameters  $M_{U_R, D_R}^i, M_{Q_L}^i$  ( $i = 1, 2, 3$ ), the trilinear couplings  $A_t, A_b, A_\tau$ , and the slepton mass parameters  $M_E^i, M_L^i$ . We set  $A_b, A_\tau$ , squark and slepton mass parameters to  $2 \text{ TeV}$ . In order to maximize the one-loop top/stop contributions to the lightest  $CP$ -even Higgs mass, the trilinear soft coupling  $A_t$  is varied over a

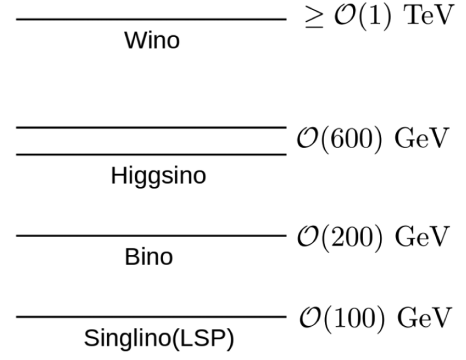


FIG. 1. Mass hierarchy in the electroweakino sector.

wide range  $[-10, 10] \text{ TeV}$ . To respect the charge and color breaking minima [65, 66], we exploit the maximum mixing scenario (cf. Ref. [67]) and require that the ratio of stop mixing parameter  $|X_t|$  ( $= A_t - \mu \cot \beta$ ) to average stop mass  $M_T$  ( $M_T^2 = m_{\tilde{t}_1, \tilde{t}_2}$ , where  $m_{\tilde{t}_1, \tilde{t}_2}$  are the stop masses) to satisfy  $|X_t/M_T| < 2.5$  [66, 68].

### A. Scan range

We utilize the NMSSMTOOLS-5.5.3 [69, 70] package to perform a random scan over the parameter space. The particle masses, couplings, branching ratios, and decay widths are also computed using NMSSMTOOLS-5.5.3. We perform a flat random scan over  $10^8$  points. The efficiency for obtaining allowed parameter space consistent with the current collider and astrophysical data (discussed in Sec. III B) is 0.001%. The scan is performed over the following range of input parameters:

$$\begin{aligned} 10^{-5} < \lambda < 0.1, \quad \left| \frac{\kappa}{\lambda} \right| \leq 0.15, \quad M_1 = (150, 550) \text{ GeV}, \\ M_2 = (2000, 3000) \text{ GeV}, \quad M_3 = (3000, 10000) \text{ GeV}, \\ \mu = (500, 1000) \text{ GeV}, \quad \tan \beta = (1, 40), \\ A_\lambda = (-100, 10000) \text{ GeV}, \quad A_\kappa = (-1000, 100) \text{ GeV}, \\ A_t = (-10000, 10000) \text{ GeV}. \end{aligned} \quad (3.2)$$

### B. Constraints

As discussed previously, the lightest  $CP$ -even Higgs boson  $H_1$  plays the role of the observed SM-like Higgs boson. In this regard,  $H_1$  is required to be consistent with the Higgs mass constraints and Higgs signal strength constraints coming from the LHC. The heavier  $CP$ -even Higgs bosons  $H_2, H_3$  and the  $CP$ -odd Higgs bosons  $A_1, A_2$  can be an admixture of singlet and doublet components and can be constrained by heavy Higgs searches at the LHC. The constraints from heavy Higgs searches are subject to the doublet content and get weaker with increasing singlet admixture. Furthermore, the NMSSM parameter space of

our interest is also constrained by limits from LEP searches, flavor physics, direct and indirect detection experiments, and direct electroweakino searches at the LHC. We discuss various constraints below.

- (1) Mass of SM-like Higgs boson: The mass of the observed Higgs boson has been measured to be within 124.4–125.8 GeV at  $3\sigma$  uncertainty [71]. Acknowledging the theoretical uncertainties in Higgs mass computation [72–74], and adopting a conservative approach, we allow  $m_{H_1}$  to lie within the range  $122 \text{ GeV} \leq m_{H_1} \leq 128 \text{ GeV}$ .
- (2) Limits from LEP: We impose a lower limit on the chargino mass  $M_{\tilde{\chi}_1^\pm} > 103.5 \text{ GeV}$ , which implies a lower bound of  $\mu, M_2 \gtrsim 100 \text{ GeV}$  [75]. Searches at LEP have also derived an upper limit of 0.1 pb on the production cross section of  $e^+e^- \rightarrow (\tilde{\chi}_2^0 \rightarrow q\tilde{q}\tilde{\chi}_1^0)\tilde{\chi}_1^0$  for  $|m_{\tilde{\chi}_2^0} - m_{\tilde{\chi}_1^0}| > 5 \text{ GeV}$  [76]. We also require  $\Gamma_{Z_{\text{inv}}} < 2 \text{ MeV}$  [77], where  $\Gamma_{Z_{\text{inv}}}$  is the invisible decay width for the  $Z$  boson excluding neutrinos. These constraints have been imposed using the NMSMTOOLS-5.5.3 package.
- (3) Constraints from Higgs signal strength measurements: Measurements by the ATLAS and CMS collaborations of the couplings of the 125 GeV Higgs boson with SM particles are encoded via signal strength parameters  $\mu_i^f$  defined as

$$\mu_i^f = \frac{\sigma_i \times \text{BR}^f}{(\sigma_i)_{\text{SM}} \times (\text{BR}^f)_{\text{SM}}}. \quad (3.3)$$

Here,  $i$  represents the various production modes of the Higgs boson viz. gluon fusion ( $ggF$ ), vector boson fusion ( $VBF$ ), associated production with vector bosons ( $VH$  ( $V = W^\pm, Z$ )), while  $f$  denotes the various decay modes of the Higgs viz.  $b\bar{b}, \gamma\gamma, \tau^+\tau^-, ZZ^*, W^+W^{*-}$ . In the present analysis, signal strength measurements for  $\{i = ggF, f = \gamma\gamma, W^+W^-, b\bar{b}, \tau\tau, ZZ\}$ ,  $\{i = VBF, f = \gamma\gamma, \tau\tau\}$ , and  $\{i = VH, f = W^+W^-, b\bar{b}\}$  [78–83] have been implemented through a global  $\chi^2$  fit assuming  $2\sigma$  uncertainty following the strategy in Ref. [84].

- (4) Constraints from flavor physics: The flavor physics constraints are imposed through bounds on the branching ratios of relevant rare processes viz.  $\text{Br}(b \rightarrow s\gamma)$ ,  $\text{Br}(B_s \rightarrow \mu^+\mu^-)$ , and  $\text{Br}(B^+ \rightarrow \tau^+\nu_\tau)$ , which are sensitive to SUSY contributions. For example, the loop-mediated  $b \rightarrow s\gamma$  process is sensitive to modifications from loops involving charged Higgs-top, neutral Higgs-bottom, and electroweakino-squark contributions. Contributions from the latter decouple since the squark masses have been fixed at a rather high value  $\sim 2 \text{ TeV}$ . The  $B_s \rightarrow \mu^+\mu^-$  process is mediated through penguin and box diagrams at one loop. Both contributions are

sensitive to a loop containing scalar or pseudoscalar heavy Higgs and a down quark. The contributions from the penguin diagram are also sensitive to modifications from loops containing charged Higgs-up quark, Higgsino-up quark, and gaugino-up quark, while loops from up quark-charged Higgs-neutrino, up squark-charged Higgsino-sneutrino, and up squark-charged wino-sneutrino contributions can induce modifications to the box diagram contributions. Recent measurements are  $\text{Br}(B \rightarrow X_s\gamma) = (3.32 \pm 0.15) \times 10^{-4}$  [85],  $\text{Br}(B_s \rightarrow \mu^+\mu^-) = (2.69_{-0.35}^{+0.37}) \times 10^{-9}$  [86,87], and  $\text{Br}(B^+ \rightarrow \tau^+\nu) = (1.06 \pm 0.19) \times 10^{-4}$  [85]. We use micROMEGAS-5.0.8 [88–90] to compute the corresponding branching ratios for points in our allowed parameter space and require them to fall within  $2\sigma$  uncertainty of the current best-fit values. We also include a theoretical uncertainty of 10% while computing the  $1\sigma$  ranges. Constraints on  $\Delta M_D, \Delta M_S$ , the mass differences between  $B_d^0, \bar{B}_d^0$  and  $B_s^0, \bar{B}_s^0$  respectively, are also imposed through the NMSMTOOLS-5.5.3 package.

- (5) Constraints from LHC searches: The composition of heavy Higgs bosons  $H_2$  and  $A_1$  in the parameter space of interest are presented in Figs. 2 (left) and 2 (right), respectively. In Fig. 2,  $S_{21}^2 + S_{22}^2$  and  $S_{23}^2$  represents the doublet and singlet content in  $H_2$ . Similarly, the doublet and singlet admixture in  $A_1$  is denoted by  $P_{11}^2$  and  $P_{12}^2$ , respectively. We observe that both  $H_2$  and  $A_1$  have a dominant singlino composition ( $\gtrsim 90\%$ ), leading to immunity from heavy Higgs search limits. We would like to note that the heaviest neutral Higgses  $H_3$  and  $A_2$  have a dominant doublet composition and have masses above  $\gtrsim 2 \text{ TeV}$ , thereby remaining outside the direct reach of current LHC. Searches for long-lived particles at the LHC can also potentially constrain the allowed parameter space. We discuss their impact for some benchmark scenarios in Sec. V D.

Searches for pair-produced electroweakinos in the hadronic final state by the ATLAS collaboration using LHC run-II data collected at  $\mathcal{L} = 139 \text{ fb}^{-1}$  have excluded winos (Higgsinos) up to a mass of 1060 GeV (900 GeV) given  $m_{\tilde{\chi}_1^0} \leq 400 \text{ GeV}$  (240 GeV) and the mass difference between the decaying wino (Higgsino) and the LSP is larger than 400 GeV (450 GeV) at 95% C.L. [27]. However, these searches assume a simplified framework where the heavier wino/Higgsinolike electroweakinos  $\tilde{\chi}_i^0$  directly decay into the LSP  $\tilde{\chi}_1^0$  with  $\text{Br}(\tilde{\chi}_i^0 \rightarrow \tilde{\chi}_1^0 + Z) + \text{Br}(\tilde{\chi}_i^0 \rightarrow \tilde{\chi}_1^0 + h_{125}) = 100\%$ . Let us analyze the implications of these constraints on the parameter space considered in this work. Within the parameter space of our interest,  $\tilde{\chi}_3^0, \tilde{\chi}_4^0$ , and  $\tilde{\chi}_1^\pm$  have dominant Higgsino composition with masses ranging from

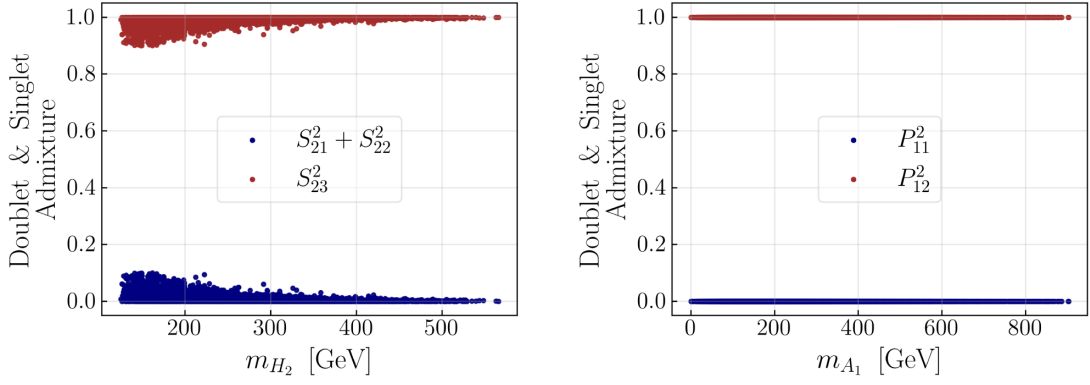


FIG. 2. Singlet and doublet admixtures in  $H_2$  (left panel) and  $A_1$  (right panel) for parameter space allowed by light Higgs mass constraints, LEP limits, Higgs signal strength constraints and bounds from flavor physics.  $S_{21}^2 + S_{22}^2$  and  $S_{23}^2$  correspond to the doublet and singlet admixtures, respectively, in  $H_2$ .  $P_{11}^2$  and  $P_{12}^2$  represent the doublet and singlet admixture, respectively, in  $A_1$ .

$\sim 500$  GeV to 2 TeV, while the winolike  $\tilde{\chi}_5^0$  and  $\tilde{\chi}_2^\pm$  are decoupled  $m_{\tilde{\chi}_5^0/\tilde{\chi}_2^\pm} \gtrsim 2$  TeV. In principle,  $\tilde{\chi}_3^0, \tilde{\chi}_4^0$ , and  $\tilde{\chi}_1^\pm$  have two potential pathways for decay, either through the intermediate binolike  $\tilde{\chi}_2^0$  or directly into the singlinolike  $\tilde{\chi}_1^0$ . The partial decay width for  $\tilde{\chi}_3^0/\tilde{\chi}_4^0 \rightarrow \tilde{\chi}_1^0 Z^*$  is determined by the Higgsino admixture in  $\tilde{\chi}_1^0$ , which is directly proportional to  $\lambda$ . The partial decay width for  $\tilde{\chi}_3^0/\tilde{\chi}_4^0 \rightarrow \tilde{\chi}_1^0 H$  also has a similar  $\lambda$  dependence by virtue of the second term in the NMSSM superpotential in Eq. (2.1). Therefore, the partial decay widths for both channels through which  $\tilde{\chi}_3^0/\tilde{\chi}_4^0$  can directly decay into  $\tilde{\chi}_1^0$  are  $\mathcal{O}(\lambda^2)$  [91]. Thus, they are far smaller relative to the partial decay widths for  $\tilde{\chi}_3^0/\tilde{\chi}_4^0$  decaying into the binolike  $\tilde{\chi}_2^0$ . Similar arguments can also be extended to the Higgsinolike  $\tilde{\chi}_1^\pm$ . Consequently, in the present scenario, directly produced  $pp \rightarrow \tilde{\chi}_3^0 \tilde{\chi}_1^\pm + \tilde{\chi}_4^0 \tilde{\chi}_1^\pm$  will dominantly undergo cascade decay via  $(\tilde{\chi}_3^0/\tilde{\chi}_4^0 \rightarrow (\tilde{\chi}_2^0 \rightarrow \tilde{\chi}_1^0 Z^{(*)}/H^{(*)})Z/H)(\tilde{\chi}_1^\pm \rightarrow (\tilde{\chi}_2^0 \rightarrow \tilde{\chi}_1^0 Z^{(*)}/H^{(*)})W^\pm)$  leading to final states that are markedly different from those considered in the ATLAS search [27]. Furthermore, the allowed points in the parameter space with  $m_{\tilde{\chi}_3^0, \tilde{\chi}_4^0, \tilde{\chi}_1^\pm} \lesssim 1$  TeV and a dominant Higgsino admixture in  $\tilde{\chi}_3^0, \tilde{\chi}_4^0$  and  $\tilde{\chi}_1^\pm$  ( $\gtrsim 90\%$ ), correspond to mass differences between  $\{\tilde{\chi}_3^0/\tilde{\chi}_4^0/\tilde{\chi}_1^\pm\}$  and  $\tilde{\chi}_2^0$ , which are very close to the ATLAS search threshold  $\sim 400$  GeV [27], leading to low efficiencies. Overall, the parameter space of our interest is rather weakly constrained by all the direct electroweakino searches at the LHC.

- (6) Constraints from direct detection: We apply the most recent upper limits on spin-independent (SI) WIMP-nucleon interaction cross section  $\sigma_{\text{SI}}$  from Xenon-1T [92] and PandaX [93], on spin-dependent (SD) WIMP-proton interaction cross section  $\sigma_{\text{SD}_p}$  from PICO-60 [94] and SD WIMP-neutron

interaction cross section  $\sigma_{\text{SD}_n}$  from Xenon-1T [95]. We impose these direct detection (DD) limits after all the constraints discussed till now and find that these direct detection searches do not lead to any additional constraints on the parameter space. In fact, the predicted SI DD cross-sections fall below the neutrino floor for the entirety of the currently allowed points in the scanned parameter space. Hence, these would be inaccessible to future DD experiments based on  $\sigma_{\text{SI}}$  measurements. We also examine the projected sensitivity at the future  $\sigma_{\text{SD}}$  based experiments. For the range of  $m_{\tilde{\chi}_1^0}$  in the parameter space of our interest, the most stringent projected sensitivities for  $\sigma_{\text{SD}_p}$  and  $\sigma_{\text{SD}_n}$  are furnished by PICO-250 [96] and LZ [97], respectively. However, we observe that neither of them would be sensitive to any of the currently allowed points in the parameter space.

Having discussed the implications of the relevant current constraints, we move on to discuss the features of the currently allowed parameter space in the next section.

#### IV. FEATURES OF THE ALLOWED PARAMETER SPACE

In this section, we examine the features of the allowed parameter space. We would like to emphasize again that our objective is to delineate the NMSSM parameter space that contains a long-lived binolike  $\tilde{\chi}_2^0$  with mass  $\sim \mathcal{O}(100)$  GeV and is also allowed by the current experimental constraints. In Fig. 3, we present the fraction of singlino content in  $\tilde{\chi}_1^0$  (upper left), bino content in  $\tilde{\chi}_2^0$  (upper right) and Higgsino contents in  $\tilde{\chi}_3^0$  (lower left), and  $\tilde{\chi}_4^0$  (lower right) for the allowed points. We observe that the singlino admixture in  $\tilde{\chi}_1^0$  is  $\gtrsim 99\%$  while  $\tilde{\chi}_2^0$  has a dominant bino content. Similarly, the heavier neutralinos  $\tilde{\chi}_3^0$  and  $\tilde{\chi}_4^0$  have a dominant Higgsino composition.

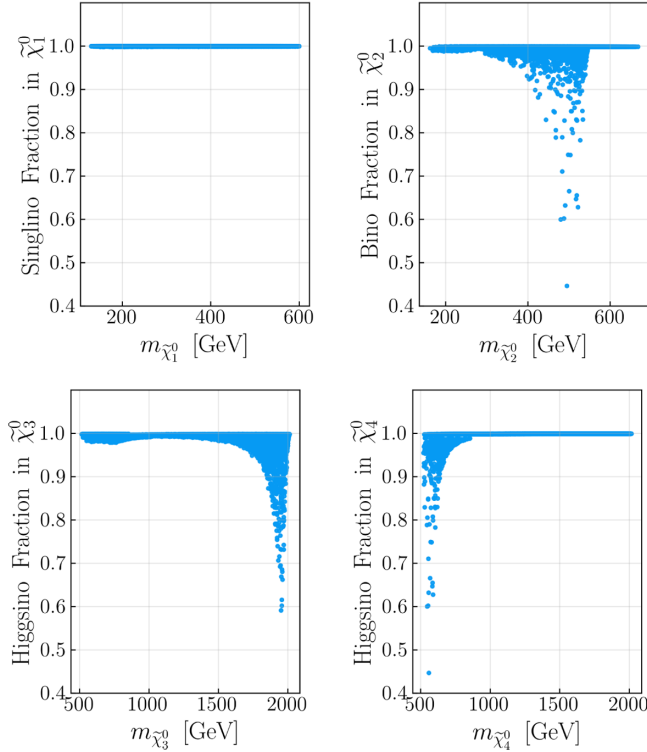


FIG. 3. Singlino content  $N_{11}^2$  in  $\tilde{\chi}_1^0$ , bino content  $N_{21}^2$  in  $\tilde{\chi}_2^0$ , Higgsino content ( $N_{33}^3 + N_{34}^2$ ) in  $\tilde{\chi}_3^0$  and Higgsino content ( $N_{43}^2 + N_{44}^2$ ) in  $\tilde{\chi}_4^0$  is shown for currently allowed parameter space.

As noted in Eq. (3.2), we consider  $|\kappa|/\lambda < 0.15$  besides  $500 \text{ GeV} \leq \mu \leq 1 \text{ TeV}$  and  $2 \text{ TeV} \leq M_2 \leq 3 \text{ TeV}$  in order to obtain a dominantly singlinolike LSP. We illustrate the allowed points in the  $k/\lambda$  vs  $\mu$  plane in the left panel of Fig. 4. The color palette represents the mass of  $\tilde{\chi}_1^0$ . We observe that  $m_{\tilde{\chi}_1^0}$  increases moderately with  $\mu$  for a fixed value of  $\kappa/\lambda$ . At a given  $\kappa/\lambda$ ,  $\kappa$  also increases with  $\mu$  since  $\mu \sim \lambda v_S$ . This leads to an increment in the mass of singlinolike  $\tilde{\chi}_1^0$  since  $m_{\tilde{\chi}_1^0} \sim 2\kappa v_S$ . For a fixed  $\mu$ , the points with the smallest values of  $|\kappa|/\lambda$  correspond to lowest,  $m_{\tilde{\chi}_1^0}$  as implied from Eq. (3.1).<sup>1</sup> Considering  $\mu \sim 1 \text{ TeV}$  and our assumption of  $|\kappa|/\lambda < 0.15$ ,  $m_{\tilde{\chi}_1^0}$  is restricted to  $m_{\tilde{\chi}_1^0} \lesssim 300 \text{ GeV}$ , which is consistent with the observations in Fig. 4 (left). Similarly, at  $\mu \sim 1 \text{ TeV}$ , the lowest value of  $m_{\tilde{\chi}_1^0}$ ,  $m_{\tilde{\chi}_1^0} \sim 125 \text{ GeV}$ , implies a lower limit of  $|\kappa|/\lambda \gtrsim 0.063$ . As we move towards smaller values of  $\mu$ , the lower limit on  $|\kappa|/\lambda$  gets stronger, for instance at  $\mu \sim 500 \text{ GeV}$ , we obtain  $|\kappa|/\lambda \gtrsim 0.125$  for  $m_{\tilde{\chi}_1^0} \sim 125 \text{ GeV}$ , as also observed in Fig. 4 (left). We also present the allowed points in the  $\kappa$  vs.  $A_\kappa$  plane in the right panel of Fig. 4. While both  $\kappa$  and  $A_\kappa$  can take positive or negative values,

<sup>1</sup>Equation (3.1) can be adapted to  $|\kappa|/\lambda \sim 0.5 \times m_{\tilde{\chi}_1^0}/\mu$ , which shows a direct correlation between  $m_{\tilde{\chi}_1^0}$  and  $|\kappa|/\lambda$  at a given  $\mu$ .

their product is required to be  $\lesssim 0$ . This requirement is implied by Eq. (2.7) where a positive value of  $M_{P,22}^2$  at small  $\lambda$  is guaranteed only if  $\kappa A_\kappa < 0$ . One of the most exciting aspects of the parameter space is the presence of a long-lived neutralino. In Fig. 5, we present the decay width of  $\tilde{\chi}_2^0$  ( $\Gamma_{\tilde{\chi}_2^0}$ ) as a function of the mass difference between  $\tilde{\chi}_2^0$  and  $\tilde{\chi}_1^0$ ,  $\Delta m(\tilde{\chi}_2^0 - \tilde{\chi}_1^0)$ . We concentrate on the region highlighted pink with  $\Gamma_{\tilde{\chi}_2^0} \leq 10^{-13}$ . A decay width of  $\Gamma \sim 10^{-13} \text{ GeV}$  roughly translates to  $c\tau \sim \mathcal{O}(0.1) \text{ mm}$ . We observe that  $\Gamma_{\tilde{\chi}_2^0}$  can be smaller than  $\lesssim 10^{-13} \text{ GeV}$  when  $\Delta m(\tilde{\chi}_2^0 - \tilde{\chi}_1^0) < m_Z$ . In this region, only three body decays of  $\tilde{\chi}_2^0$  are viable [98]. We observe that  $\Gamma_{\tilde{\chi}_2^0}$  can be as small as  $\sim 10^{-19} \text{ GeV}$  for relatively smaller mass differences  $\Delta m(\tilde{\chi}_2^0 - \tilde{\chi}_1^0) \lesssim 40 \text{ GeV}$ . Most notably, this mass difference is still large enough to produce energetic final states as  $\tilde{\chi}_2^0$  decays. Such configurations are not possible in MSSM with neutralino LSP and are a unique feature of the NMSSM scenario we consider.

Thus, the allowed points can have long-lived binolike  $\tilde{\chi}_2^0$  with decay widths up to  $\sim 10^{-19} \text{ GeV}$ . Furthermore, the heavier neutralinos  $\tilde{\chi}_3^0, \tilde{\chi}_4^0$  and the lightest chargino  $\tilde{\chi}_1^\pm$  have a dominant Higgsino admixture while  $\tilde{\chi}_5^0$  and  $\tilde{\chi}_2^\pm$  are winolike. We have set  $M_2$  to be above  $\gtrsim 2 \text{ TeV}$ , thus, decoupling  $\tilde{\chi}_5^0$  and  $\tilde{\chi}_2^\pm$  from the rest of the electroweakinos. Since the LSP  $\tilde{\chi}_1^0$  has a dominant singlino content, the Higgsinolike  $\tilde{\chi}_3^0, \tilde{\chi}_4^0$  mostly decays through the intermediate binolike  $\tilde{\chi}_2^0$ ,  $\tilde{\chi}_3^0/\tilde{\chi}_4^0 \rightarrow \tilde{\chi}_2^0 + H_1/Z$ , instead of decaying directly into  $\tilde{\chi}_1^0 + X$  states. In Fig. 6, we present the branching ratios  $\text{Br}(\tilde{\chi}_3^0 \rightarrow \tilde{\chi}_2^0 + H_1/Z)$  (upper-left panel) and  $\text{Br}(\tilde{\chi}_4^0 \rightarrow \tilde{\chi}_2^0 + H_1/Z)$  (upper-right panel) for the allowed parameter space. We observe that  $\tilde{\chi}_3^0$  ( $\tilde{\chi}_4^0$ ) can decay via  $\tilde{\chi}_2^0 + H_1$  ( $\tilde{\chi}_2^0 + Z$ ) with branching fractions as large as  $\sim 0.9$ . The  $\tilde{\chi}_2^0$  s can eventually undergo three-body decay,

$$\tilde{\chi}_2^0 \rightarrow \tilde{\chi}_1^0 + Y, \quad (4.1)$$

where  $Y = b\bar{b}, \tau^\pm\tau^\mp, \ell^\pm\ell^\mp, j\bar{j}$ , mediated through off-shell  $Z$  or Higgs boson if  $\Delta(\tilde{\chi}_2^0 - \tilde{\chi}_1^0) < m_Z$ . Here  $\ell$  represents electrons and muons. The correlations among the three-body branching ratios of  $\tilde{\chi}_2^0$  in various decay modes for the allowed parameter space points are shown in Fig. 6 (lower panel). Points with  $\kappa > 0$  and  $\kappa < 0$  are represented in blue and red colors, respectively. In the  $\kappa < 0$  scenario, the three-body decays of  $\tilde{\chi}_2^0$  are dominantly mediated through  $Z^*$ , resulting in generation universal branching fractions in leptonic decay modes. The  $Z$  mediated coupling  $g_{Z\tilde{\chi}_1^0\tilde{\chi}_2^0}$  is governed by the Higgsino admixtures  $g_{Z\tilde{\chi}_1^0\tilde{\chi}_2^0} \sim (N_{i3}N_{j3} - N_{j4}N_{k4})$ . In the parameter space of our interest, we observe that the Higgsino fractions in  $\tilde{\chi}_1^0$  are typically larger by 1–3 orders of magnitude in the  $\kappa < 0$  scenario compared to that

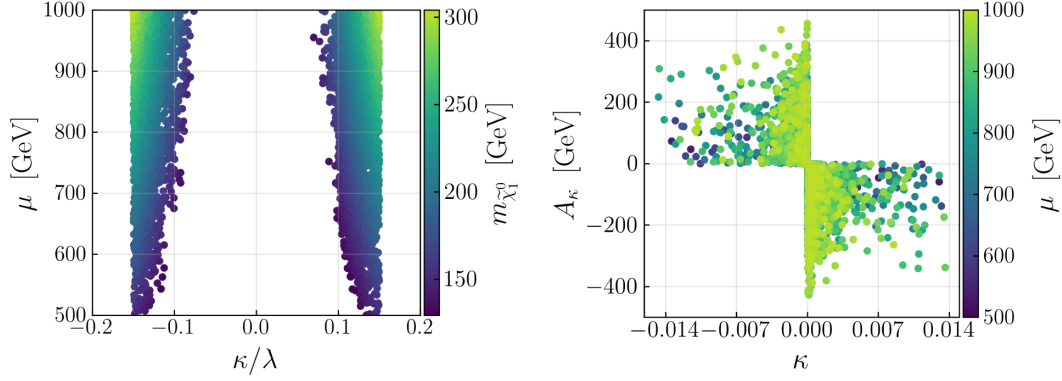


FIG. 4. Left panel: allowed parameter space points in the plane of  $\kappa/\lambda$  vs.  $\mu$ . The color palette represents the mass of the singlinlike LSP neutralino. Right panel: allowed parameter space in the  $k$  vs.  $A_k$  plane. The color palette represents the Higgsino mass parameter  $\mu$ .

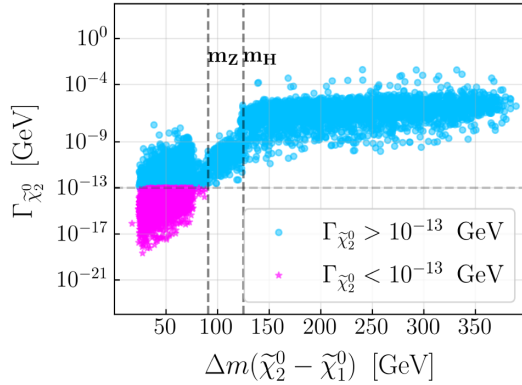


FIG. 5. Allowed parameter space are presented in the plane of mass difference between  $\tilde{\chi}_2^0$  and  $\tilde{\chi}_1^0$   $\Delta m(\tilde{\chi}_2^0 - \tilde{\chi}_1^0)$  vs. the decay width of  $\tilde{\chi}_2^0$   $\Gamma_{\tilde{\chi}_2^0}$ . The vertical black dashed lines represent the  $Z$  and  $H_{125}$  on-shell conditions. Parameter space with  $\Gamma_{\tilde{\chi}_2^0} \leq 10^{-13}$  GeV and  $\Gamma_{\tilde{\chi}_2^0} > 10^{-13}$  GeV are illustrated in pink and cyan colors, respectively.

in the  $\kappa > 0$  case, giving more precedence to  $Z$  over  $h$  mediated decays.

## V. DISCOVERY POTENTIAL OF LLP DECAYS AT THE HL-LHC

### A. Electroweakino pair production rates at the HL-LHC

As discussed previously, directly produced chargino-neutralino pairs at the HL-LHC can lead to interesting final state topologies involving long-lived  $\tilde{\chi}_2^0$  in addition to several promptly decaying candidates. Such typical cascade decay chain can be written as follows:

$$\begin{aligned}
 pp &\rightarrow \tilde{\chi}_1^\pm \tilde{\chi}_3^0 + \tilde{\chi}_1^\pm \tilde{\chi}_4^0, \\
 \tilde{\chi}_1^\pm &\rightarrow \tilde{\chi}_2^0 + W^\pm, & \tilde{\chi}_2^0 &\rightarrow \tilde{\chi}_1^0 + Y, \\
 \tilde{\chi}_3^0/\tilde{\chi}_4^0 &\rightarrow \tilde{\chi}_2^0 + Z/H_1, & \tilde{\chi}_2^0 &\rightarrow \tilde{\chi}_1^0 + Y,
 \end{aligned} \quad (5.1)$$

where  $Y$  represents all possible visible final states produced from the decay of  $\tilde{\chi}_2^0$  i.e.,  $Y = b\bar{b}, \tau^\pm \tau^\mp, \ell^\pm \ell^\mp, j\bar{j}$ . Since the  $\tilde{\chi}_2^0$  is long lived, the final states contain displaced jets or leptons along with  $W + Z/H_1 + \cancel{E}_T$ . Henceforth, we refer to all possible visible decay modes of  $\tilde{\chi}_2^0$  as  $Y$ . For illustration, we show a typical leading order Feynman diagram in Fig. 7 (left).

The direct production of a chargino-neutralino pair is a pure electroweak process and is controlled by the  $W^\pm \tilde{\chi}_i^\pm \tilde{\chi}_j^0$  coupling. We obtain the production cross sections  $\sigma(pp \rightarrow \tilde{\chi}_1^\pm \tilde{\chi}_3^0 + \tilde{\chi}_1^\pm \tilde{\chi}_4^0)$  for configurations of our interest by rescaling the next-to-leading-order (NLO) MSSM production cross sections computed using PROSPINO [99] for a pure Higgsinlike  $\tilde{\chi}_i^\pm \tilde{\chi}_j^0$  as follows:

$$\begin{aligned}
 C_{W\tilde{\chi}_i^\pm \tilde{\chi}_j^0}^2 \Big|_{j=3,4} &= \{(N_{j3}V_{12} - \sqrt{2}N_{j2}V_{11})^2 \\
 &+ (N_{j4}U_{12} + \sqrt{2}N_{j2}U_{11})^2\}. \quad (5.2)
 \end{aligned}$$

Here,  $N_{j3/j4}$  represents the Higgsino component while  $N_{j2}$  denotes the wino component in the  $j$ th neutralino. The Higgsino and wino admixtures in  $\tilde{\chi}_1^\pm$  are represented by  $V_{12}/U_{12}$  and  $V_{11}/U_{11}$ , respectively. The NMSSM parameter space considered in the present study characterizes a dominant Higgsino composition in  $\tilde{\chi}_3^0/\tilde{\chi}_4^0$  and  $\tilde{\chi}_1^\pm$ . Correspondingly, both  $N_{33}^2 + N_{34}^2$  and  $N_{43}^2 + N_{44}^2 \sim 1$ . Similarly,  $U_{12}$  and  $V_{12}$  are  $\sim 1$ . On the other hand,  $N_{32}$ ,  $N_{42}$ ,  $V_{11}$ , and  $U_{11}$  are  $\ll 1$ . Therefore, from Eq. (5.2)  $(N_{j3}V_{12})^2$  and  $(N_{j4}U_{12})^2$  are the only relevant terms to compute  $\sigma(pp \rightarrow \tilde{\chi}_1^\pm \tilde{\chi}_3^0 + \tilde{\chi}_1^\pm \tilde{\chi}_4^0)$ . The scaled production cross section is then multiplied by the relevant branching ratios for  $\tilde{\chi}_2^0$ ,  $H_1/Z$  and  $W^\pm$ . In Fig. 7 (right), for all the allowed points featuring a long-lived  $\tilde{\chi}_2^0$  (Fig. 5, pink points) we present a cross section ( $\sigma(pp \rightarrow \tilde{\chi}_1^\pm \tilde{\chi}_3^0 + \tilde{\chi}_1^\pm \tilde{\chi}_4^0) \times \text{Br}(\tilde{\chi}_1^\pm \rightarrow \tilde{\chi}_2^0 + W^\pm, \tilde{\chi}_2^0 \rightarrow \tilde{\chi}_1^0 + Y) \times \text{Br}(\tilde{\chi}_3^0/\tilde{\chi}_4^0 \rightarrow \tilde{\chi}_2^0 + H_1/Z, \tilde{\chi}_2^0 \rightarrow \tilde{\chi}_1^0 + Y)$ ) at  $\sqrt{s} = 14$  TeV as a function of  $m_{\tilde{\chi}_3^0}$ . This cross section of the entire cascade chain can be

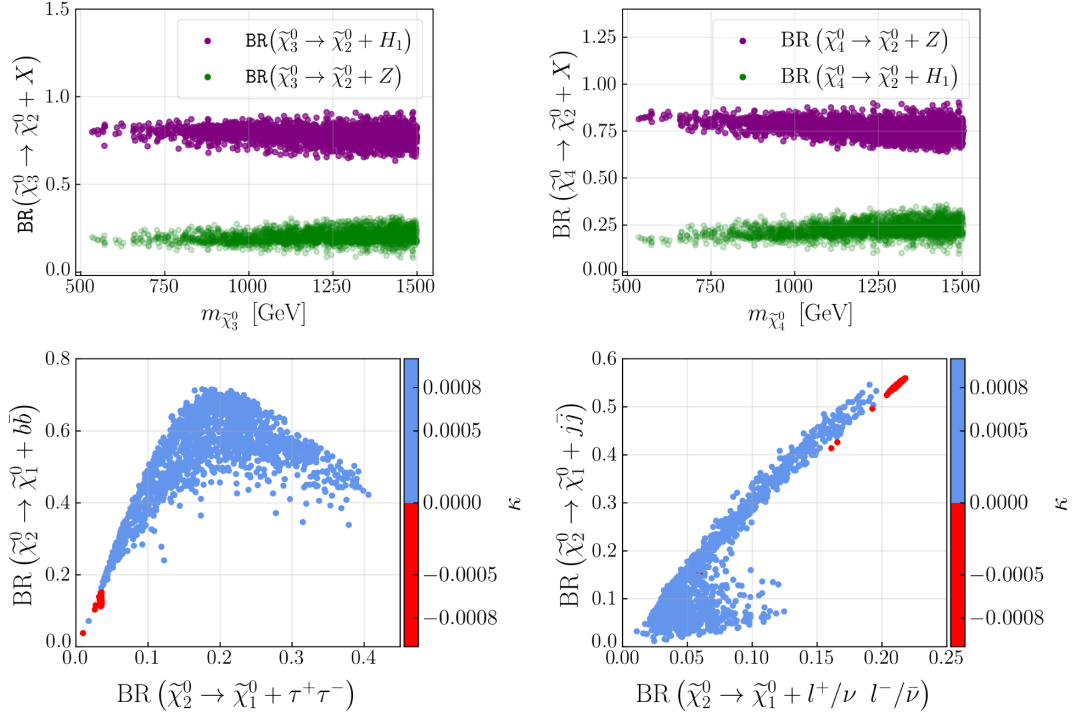


FIG. 6. Upper panel: branching fractions for the dominant decay modes of  $\tilde{\chi}_3^0$  (left) and  $\tilde{\chi}_4^0$  (right) are shown for allowed parameter space. The green and purple colored points represent the branching ratio of  $\tilde{\chi}_3^0/\tilde{\chi}_4^0$  into  $\tilde{\chi}_2^0 + Z$  and  $\tilde{\chi}_2^0 + H_1$ , respectively. Lower panel: correlations among the branching fractions for  $\tilde{\chi}_2^0$ ,  $\{\text{BR}(\tilde{\chi}_2^0 \rightarrow \tilde{\chi}_1^0 + b\bar{b}), \text{BR}(\tilde{\chi}_2^0 \rightarrow \tilde{\chi}_1^0 + \tau\tau)\}$  (left) and  $\{\text{BR}(\tilde{\chi}_2^0 \rightarrow \tilde{\chi}_1^0 + \text{jets}), \text{BR}(\tilde{\chi}_2^0 \rightarrow \tilde{\chi}_1^0 + \ell^\pm \ell^\mp / \nu \bar{\nu})\}$  (right), are shown for the allowed parameter space points with  $\kappa > 0$  (blue) and  $\kappa < 0$  (red).

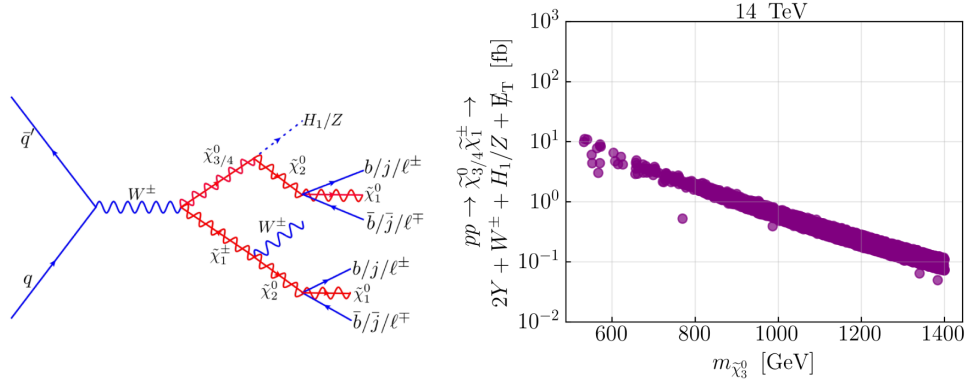


FIG. 7. Left panel: Feynman diagram at the leading order for the signal process  $\tilde{\chi}_1^\pm \tilde{\chi}_3^0/\tilde{\chi}_4^0 \rightarrow (\tilde{\chi}_1^\pm \rightarrow \tilde{\chi}_2^0 + W^\pm, \tilde{\chi}_2^0 \rightarrow \tilde{\chi}_1^0 + Y) \times (\tilde{\chi}_3^0/\tilde{\chi}_4^0 \rightarrow \tilde{\chi}_2^0 + H_1/Z, \tilde{\chi}_2^0 \rightarrow \tilde{\chi}_1^0 + Y)$ . Right panel: Leading order cross section for the process  $pp \rightarrow \tilde{\chi}_1^\pm \tilde{\chi}_3^0/\tilde{\chi}_4^0 \rightarrow (\tilde{\chi}_1^\pm \rightarrow \tilde{\chi}_2^0 + W^\pm, \tilde{\chi}_2^0 \rightarrow \tilde{\chi}_1^0 + Y)(\tilde{\chi}_3^0/\tilde{\chi}_4^0 \rightarrow \tilde{\chi}_2^0 + H_1/Z, \tilde{\chi}_2^0 \rightarrow \tilde{\chi}_1^0 + Y) \rightarrow 2Y + WH_1/Z + \cancel{E}_T$  at  $\sqrt{s} = 14$  TeV for the allowed parameter space with  $\Gamma_{\tilde{\chi}_2^0} < 10^{-13}$  GeV. Here,  $Y$  corresponds to all visible decays of  $\tilde{\chi}_2^0$ , viz.  $Y = b\bar{b}, \tau^\pm \tau^\mp, \ell^\pm \ell^\mp, j\bar{j}$ .

as large as  $\mathcal{O}(1)$  fb and  $\mathcal{O}(0.1)$  fb at  $m_{\tilde{\chi}_3^0} \sim 500$  GeV and  $\sim 1$  TeV, respectively. Considering the large production rates at the HL-LHC, we perform a detailed collider study to explore the projected sensitivity for some benchmark scenarios selected from the allowed parameter space. We focus on direct electroweakino production with the final state containing  $WZ/H_1 + \cancel{E}_T$  + displaced objects. Before moving to a discussion of the details of the collider

analysis, let us examine some generic features of long-lived particles that are relevant to the present study.

## B. Kinematic features of LLP decays

In Fig. 8 (left), we illustrate allowed parameter space with  $\Gamma_{\tilde{\chi}_2^0} \leq 10^{-13}$  GeV (Fig. 5, pink points) in the plane of mean proper decay length,  $c\tau_{\tilde{\chi}_2^0}^0$  vs. mass of the LLP  $\tilde{\chi}_2^0$ .

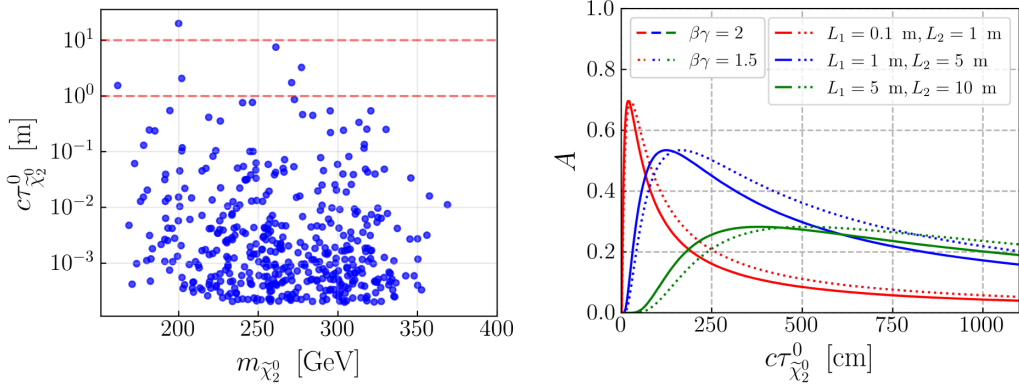


FIG. 8. Left panel: decay length of the LLP as a function of its mass. The top and bottom red horizontal lines correspond to a decay length of 10 and 1 m, respectively. This shows that the SM decay products of LLP can reach the electromagnetic calorimeter (ECAL) and can also traverse a few meters in HCAL. For lengths  $\geq \mathcal{O}(10)$  m, they can even reach the muon detectors. Right panel: acceptance probability of an LLP with constant boost,  $A$  in Eq. (5.7) vs. decay length of that LLP  $\tilde{\chi}_2^0$ ,  $c\tau_{\tilde{\chi}_2^0}^0$  for three choices of  $\{L_1, L_2\}$ :  $\{0.1 \text{ m}, 1 \text{ m}\}$ ,  $\{1 \text{ m}, 5 \text{ m}\}$ , and  $\{5 \text{ m}, 10 \text{ m}\}$ , assuming a hypothetical scenario with  $\beta\gamma = 2$  and 1.5. Here,  $L_1$  and  $L_2$  are the inner and outer radii of the LLP sensitive detector volume.

Here,  $\tau_{\tilde{\chi}_2^0}$  represents the mean proper lifetime of  $\tilde{\chi}_2^0$ , and  $c$  is the speed of light. For convenience, we refer to the mean proper decay lifetime ( $\tau^0$ ) as just “lifetime” and the mean proper decay length ( $c\tau^0$ ) as “decay length” unless stated otherwise. The decay length for  $\tilde{\chi}_2^0$  is relatively large,  $c\tau_{\tilde{\chi}_2^0}^0 \gtrsim 10$  cm, for a considerable fraction of the allowed parameter space. The decay length of  $\tilde{\chi}_2^0$  in the laboratory frame is given by

$$l_{\tilde{\chi}_2^0} = \beta\gamma c\tau_{\tilde{\chi}_2^0}^0, \quad (5.3)$$

where  $\gamma = (1 - \beta^2)^{-1/2}$  is the relativistic factor,  $\beta = |\vec{p}|/E = v/c$  is the boost,  $v$  is the velocity,  $E$  is the energy, and  $|\vec{p}|$  is the momentum of the particle in the laboratory frame. The acceptance probability of a single LLP  $\tilde{\chi}_2^0$  decaying within distance  $L_1 < L < L_2$  inside the detector can be then expressed as

$$\mathcal{P}_1(L_1, L_2, \sqrt{s}) \simeq \int db f(\sqrt{s}, b) \left[ \exp\left(\frac{-L_1}{bc\tau_{\tilde{\chi}_2^0}^0}\right) - \exp\left(\frac{-L_2}{bc\tau_{\tilde{\chi}_2^0}^0}\right) \right], \quad (5.4)$$

where  $b = \beta\gamma$ ,  $f(\sqrt{s}, b)$  is the probability density function of  $b$ ,  $L_1$  and  $L_2$  are the inner and outer radii of the detector volume that are sensitive to the LLP decay. The signal considered in the present analysis involves the decay of two long-lived  $\tilde{\chi}_2^0$ s. The probability that one decay with  $(L_1, L_2)$  and other within  $(L_3, L_4)$  is given by [100]

$$\begin{aligned} \mathcal{P}_2(L_1, L_2, L_3, L_4, \sqrt{s}) &= 2 \int db_1 db_2 f(\sqrt{s}, b_1, b_2) \\ &\times \left[ \exp\left(\frac{-L_1}{b_1 c\tau_{\tilde{\chi}_2^0}^0}\right) - \exp\left(\frac{-L_2}{b_1 c\tau_{\tilde{\chi}_2^0}^0}\right) \right] \\ &\times \left[ \exp\left(\frac{-L_3}{b_2 c\tau_{\tilde{\chi}_2^0}^0}\right) - \exp\left(\frac{-L_4}{b_2 c\tau_{\tilde{\chi}_2^0}^0}\right) \right]. \end{aligned} \quad (5.5)$$

Correspondingly, the number of observed LLP decays is given by

$$N_{\text{LLP}} = \mathcal{L} \times \sigma_{\text{signal}} \times \text{BR}^n \times \mathcal{P}_n \times \epsilon_{\text{reco}}^n, \quad (5.6)$$

where  $n$  is the number of LLPs in the decay chain,  $\mathcal{P}_n$  represents their decay probability, as given in Eq. (5.4) for one displaced secondary vertex (DSV) and Eq. (5.5) in case of two DSVs.  $\mathcal{L}$  represents the integrated luminosity,  $\sigma_{\text{signal}} \times \text{BR}^n$  refers to the event rate and  $\epsilon_{\text{reco}}^n$  corresponds to the signal efficiency. To have an idea of what detector volume is optimal for a given decay length, we consider a hypothetical scenario by setting the boost factor,  $b$ , to a constant value. Equation (5.4) with constant  $b$  reduces to

$$A = \mathcal{P}|_{b=\text{const}} \simeq \exp(-L_1/bc\tau_{\tilde{\chi}_2^0}^0) - \exp(-L_2/bc\tau_{\tilde{\chi}_2^0}^0). \quad (5.7)$$

We illustrate the variation of acceptance probability ( $A$ ) with  $c\tau_{\tilde{\chi}_2^0}^0$  in Fig. 8 (right), for three different choices of  $\{L_1, L_2\}$ :  $\{0.1 \text{ m}, 1 \text{ m}\}$ ,  $\{1 \text{ m}, 5 \text{ m}\}$ , and  $\{5 \text{ m}, 10 \text{ m}\}$ , assuming a constant  $\beta\gamma = 2$  and 1.5. For  $\{L_1 = 0.1 \text{ m}, L_2 = 1 \text{ m}\}$ , the highest acceptance probability is observed for  $c\tau_{\tilde{\chi}_2^0}^0 \sim 20$  cm. Keeping this in mind, in the analysis, we restrict the choice

TABLE I. The input parameters, Higgs boson, and electro-weakino mass spectrum, branching ratios of electroweakinos, decay width and decay length of the LLP  $\tilde{\chi}_2^0$ , and the production cross section for the process  $pp \rightarrow \tilde{\chi}_3^0 \tilde{\chi}_1^\pm + \tilde{\chi}_4^0 \tilde{\chi}_1^\pm$  at  $\sqrt{s} = 14$  TeV, for BP1, BP2, and BP3.

	BP1	BP2	BP3
$\lambda$	$5.15 \times 10^{-3}$	$5.85 \times 10^{-3}$	$1.67 \times 10^{-4}$
$\kappa$	$6.12 \times 10^{-4}$	$5.854 \times 10^{-4}$	$2.07 \times 10^{-5}$
$A_\lambda$ [GeV]	5279	2110	9705
$A_\kappa$ [GeV]	-32	-510	-21
$\mu$ [GeV]	743.05	775.05	688.05
$\tan\beta$	25.098	36.32	44.67
$M_1$ [GeV]	218.39	194.4	238.8
$M_2$ [GeV]	3909	3709	2789
$M_3$ [GeV]	4219	4371	5465
$m_{\tilde{\chi}_1^0}$ [GeV]	180.17	158.08	173.76
$m_{\tilde{\chi}_2^0}$ [GeV]	216.76	193.00	236.93
$m_{\tilde{\chi}_3^0}$ [GeV]	759.62	790.67	703.55
$m_{\tilde{\chi}_4^0}$ [GeV]	760.42	791.80	704.94
$m_{\tilde{\chi}_1^\pm}$ [GeV]	758.43	789.72	702.37
$m_{H_1}$ [GeV]	126.31	122.52	124.54
$m_{H_2}$ [GeV]	168.43	143.11	164.7
$m_{A_1}$ [GeV]	92.0	108.90	73.19
$\Gamma_{\tilde{\chi}_2^0}$ [GeV]	$1.11 \times 10^{-14}$	$7.69 \times 10^{-15}$	$3.85 \times 10^{-16}$
$\Gamma_{\tilde{\chi}_3^0}$ [GeV]	0.4847	0.5002	0.4367
$\Gamma_{\tilde{\chi}_4^0}$ [GeV]	0.4571	0.4755	0.4088
$\sigma_{\text{NLO}}$ [fb]	1.56	1.15	2.15
$\text{BR}(\tilde{\chi}_2^0 \rightarrow \tilde{\chi}_1^0 b\bar{b})$	0.528	0.63	0.34
$\text{BR}(\tilde{\chi}_2^0 \rightarrow \tilde{\chi}_1^0 j\bar{j})$	0.1834	0.074	0.3602
$\text{BR}(\tilde{\chi}_2^0 \rightarrow \tilde{\chi}_1^0 \tau^+ \tau^-)$	0.12	0.177	0.0969
$\text{BR}(\tilde{\chi}_2^0 \rightarrow \tilde{\chi}_1^0 l^+ l^-)$	0.085	0.014	0.176
$\text{BR}(\tilde{\chi}_3^0 \rightarrow \tilde{\chi}_2^0 H_1)$	0.79	0.704	0.816
$\text{BR}(\tilde{\chi}_3^0 \rightarrow \tilde{\chi}_2^0 Z)$	0.204	0.24	0.184
$\text{BR}(\tilde{\chi}_4^0 \rightarrow \tilde{\chi}_2^0 Z)$	0.7834	0.74	0.811
$\text{BR}(\tilde{\chi}_4^0 \rightarrow \tilde{\chi}_2^0 H_1)$	0.215	0.24	0.189
$\text{BR}(\tilde{\chi}_1^\mp \rightarrow \tilde{\chi}_2^0 W)$	0.994	0.995	0.999

of decay lengths of the LLP up to  $\mathcal{O}(10^1)$  cm for the benchmark points as discussed below.

The momentum resolution at the tracker is better than the energy resolution at the calorimeters for charged tracks [101]. Hence, the tracker enables more efficient identification of the charged tracks from LLP decays and reconstruction of the DSV. Keeping this in mind, in the present work, we restrict our analysis to the tracker region using single/dilepton triggers and missing energy. In both CMS and ATLAS detectors, the tracker region extends to a radius of  $L_2/L_4 \sim 1$  m. Therefore, we consider only such signal benchmark points where the decay length of  $\tilde{\chi}_2^0$ ,  $c\tau_{\tilde{\chi}_2^0}^0 \lesssim 1$  m, such that the majority of  $\tilde{\chi}_2^0$  decays occur inside

the tracker region [cf. Fig. 8 (right)]. Considering these observations, we identify three benchmark points with  $\Gamma_{\tilde{\chi}_2^0}$  (in GeV)  $\sim 10^{-14}$  (BP1),  $\sim 10^{-15}$  (BP2) and  $\sim 10^{-16}$  (BP3). In Table I, we present the input parameters, along with masses, decay widths, and branching rates of the relevant electroweakinos and Higgs bosons for BP1, BP2, and BP3.

It is worth noting that the  $\tilde{\chi}_2^0$ s in our signal benchmarks can undergo decays in different segments of the detector depending on the boost ( $\beta$ ) and decay length ( $\tau_{\tilde{\chi}_2^0}^0$ ) where the latter is inversely correlated to  $\Gamma_{\tilde{\chi}_2^0}$ . For illustration, we present the distributions for  $l_{\tilde{\chi}_2^0}$ , where  $\tilde{\chi}_2^0$  is produced via  $pp \rightarrow (\tilde{\chi}_3^0 \rightarrow \tilde{\chi}_2^0 H_1) \tilde{\chi}_1^\pm$ , for BP1 (blue solid) and BP2 (green solid), in Fig. 9. These benchmarks have  $c\tau_{\tilde{\chi}_2^0}^0 = 17.5$  mm (BP1) and 26 mm (BP2), respectively, thereby furnishing a relatively large acceptance probability in the tracker volume. We would like to note that particles with larger decay lengths can also undergo decay within the tracker region. However, the fraction of such decays would be small and warrant a separate study of its own (cf. [102]), which is beyond the scope of the present work.

As discussed previously, the decay of  $\tilde{\chi}_2^0$  to visible final states within the tracker region leads to charged tracks that originate from DSV corresponding to the LLP  $\tilde{\chi}_2^0$ . An important parameter relevant for the reconstruction of DSV is the transverse impact parameter  $|d_0|$ ,

$$|d_0| = \frac{|x_d^{\text{track}} p_y^{\text{track}} - y_d^{\text{track}} p_x^{\text{track}}|}{p_T^{\text{track}}}, \quad (5.8)$$

where  $\{x_d^{\text{track}}, y_d^{\text{track}}\}$  are the track coordinates in the transverse plane passing through the primary interaction vertex (PIV),  $p_x^{\text{track}}$  and  $p_y^{\text{track}}$  are the  $x$  and  $y$  components of the track momentum and  $p_T^{\text{track}} = \sqrt{p_x^{\text{track}2} + p_y^{\text{track}2}}$ . In the

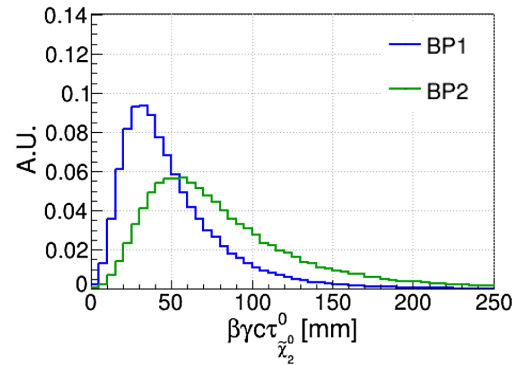


FIG. 9. Distributions for decay length of one of the LLPs  $\tilde{\chi}_2^0$  produced via  $pp \rightarrow (\tilde{\chi}_3^0 \rightarrow \tilde{\chi}_2^0 h) \tilde{\chi}_1^\pm$  at  $\sqrt{s} = 14$  TeV for signal benchmark BP1  $\{m_{\tilde{\chi}_3^0} = 760$  GeV,  $m_{\tilde{\chi}_2^0} = 217$  GeV,  $c\tau_{\tilde{\chi}_2^0}^0 = 17.5$  mm $\}$  and BP2  $\{m_{\tilde{\chi}_3^0} = 791$  GeV,  $m_{\tilde{\chi}_2^0} = 193$  GeV,  $c\tau_{\tilde{\chi}_2^0}^0 = 26$  mm $\}$  are shown as blue and green solid lines, respectively.

present scenario, the displaced charged tracks from  $\tilde{\chi}_2^0$  decays in BP1, BP2, and BP3 can feature a typically large  $|d_0| \gtrsim \mathcal{O}(1)$  cm, which is indicative of a DSV.

Note that the analysis strategy considered in this work requires separate tackling of the prompt and long-lived objects. Motivated by studies from the ATLAS and CMS collaboration in Refs. [103,104], we consider final state objects with transverse impact parameter  $d_0 \gtrsim 2$  mm to be long-lived while those with  $d_0 \lesssim 2$  mm as prompt.

### C. Benchmark points and analysis setup

Having discussed the generic features of the LLP  $\tilde{\chi}_2^0$  in a collider environment, we will move on to study the projected capability of the HL-LHC to probe the NMSSM parameter space of interest through LLP searches in direct electroweakino production of Eq. (5.1). As discussed previously, to this end, we perform a detailed collider study of three different benchmark points BP1, BP2, and BP3 (Table I), chosen from the current allowed parameter space. We use PYTHIA8 [105,106] to simulate the signal process in Eq. (5.1). The signal process is mediated through a promptly decaying  $WZ/WH_1$  in addition to the late decaying  $\tilde{\chi}_2^0$ s, leading to a variety of prompt SM objects in the final state, which could be potentially triggered upon. The list of dominant backgrounds would vary according to the trigger choice. The different viable triggers and the associated backgrounds will be discussed in detail in Sec. V E. We use the madGraph5-AMC@NLO-2.7.3 [107] framework to simulate the background events at the parton level, with subsequent showering and hadronization being performed using PYTHIA8. The HL-LHC detector response is simulated using DELPHES-3.5.0 [101] using the default HL-LHC detector card [108].

As our analysis relies on tracks originating from the LLP, we do not cluster jets but rather use DELPHES collections both for generator and reconstructed level objects within our analysis. We separate out the prompt objects like leptons, which are primarily used for event selection. The main analysis deals with displaced ‘‘particle-flow’’ tracks. The generator-level charged particles, estimated with a good resolution, have a finite probability of being reconstructed as tracks. We have checked that there is no overlap between reconstructed leptons and displaced tracks with  $|\eta| < 4$  and  $p_T > 10$  GeV in our analysis. At the stage of particle propagation, only smearing on the norm of the transverse momentum vector is applied, assuming a perfect angular resolution on tracks. In the mentioned updated Delphes module, a dedicated filter is used [109] to enhance the tracking performance along with momentum resolution. This tackles inefficiencies in boosted, dense environments. We would like to note that displaced vertex selection efficiencies for HL-LHC are not available yet and, hence, could not be applied to our analysis. Therefore, our results are optimistic estimates and should be treated as such.

### D. Sensitivity from displaced vertex searches at the LHC

Several searches for long-lived particles with displaced vertices have been performed in the literature. For example, in Refs. [110,111], searches are performed for long-lived particles decaying into displaced jets plus missing energy. Both analyses consider gauge-mediated supersymmetry breaking scenario with long-lived gluinos ( $\tilde{g}$ ), focusing on the  $pp \rightarrow \tilde{g}\tilde{g} \rightarrow \cancel{E}_T + \text{jets}$  channel, requiring one or more displaced jets and missing transverse energy in the final state. The decay topology considered in Ref. [111] can be realized in the parameter space of our interest in all electroweakino pair production modes with at least one  $\tilde{\chi}_2^0$  in the cascade decay chain,  $pp \rightarrow \tilde{\chi}_i^0 \tilde{\chi}_j^0 / \tilde{\chi}_i^\pm \tilde{\chi}_i^\mp \rightarrow \geq 1 \tilde{\chi}_2^0 + X + \cancel{E}_T$  ( $i = \{2, 3, 4\}$ ,  $j = \{1, i\}$  and  $X$  represents other promptly decaying candidates in the decay chain), provided one or more  $\tilde{\chi}_2^0$  decays into the hadronic final state resulting in displaced jets plus missing energy. Let us examine the case of BP3 where  $\tilde{\chi}_2^0$  has the largest proper decay length among the three representative benchmarks (see Table I) and closest to the decay lengths considered in the above reference. For BP3 ( $m_{\tilde{\chi}_2^0} = 237$  GeV), the production rate in the channel containing at least one displaced jet and  $\cancel{E}_T$  is  $\sim 1.435$  fb at  $\sqrt{s} = 13$  TeV. Adopting the analysis strategy from Ref. [111], we require the signal events to satisfy: (1)  $\cancel{E}_T > 300$  GeV and (2) at least one displaced vertex with an invariant mass of  $\geq 10$  GeV. Only 3% of signal events satisfy the aforementioned cuts, resulting in an effective signal production rate of  $\sigma_{BP3}^{\text{eff}} = 1.435 \text{ fb} \times 3\% = 0.04$  fb. The search in Ref. [111] excludes gluinos up to  $m_{\tilde{g}} \sim 2.1$  TeV with proper decay length between 0.3 and 30 m. The most stringent upper limit on the long-lived gluino pair production cross section times efficiency from this search is  $\sim 0.09$  fb at 95% C.L. for  $m_{\tilde{g}} = 2.4$  TeV given the proper decay length is roughly 1 m. Similarly, the search in Ref. [110] has excluded  $\sigma(pp \rightarrow \tilde{g}\tilde{g})$  up to  $\sim 0.2$  fb for  $m_{\tilde{g}} = 1.4$  and 2 TeV, at 95% C.L., with the best signal efficiency for a proper decay length of 1 m. These upper limits could be conservatively extended to smaller masses of long-lived particles. In the case of BP3, despite a smaller mass of the long-lived candidate, the production rate times signal efficiency is several factors below the current upper limit in Refs. [110,111].

It is also worth noting that extrapolating the reach of long-lived searches to the HL-LHC presents additional complexities due to challenges in devising efficient triggers for the online level (L1) and high-level trigger (HLT) amidst the high pile-up environment. Though there are not many detailed studies for dedicated LLP triggers at HL-LHC [112], CMS has explored two L1 triggers; including tracking information up to  $|d_0| = 8$  cm and ECAL barrel timing [113]. For a lighter LLP and hence with less energetic hadronic decay products, these additional advancements become more useful. Applications of

these triggers in different LLP models are still developing for both L1 and the HLT [112,114] at the HL-LHC. We opt for a standard L1 trigger, like the single lepton, in our analysis because of the advantages of similar thresholds at the L1 trigger and the HLT, inclusiveness, and less susceptibility to pileup effects. We discuss this in detail in Sec V E.

ATLAS and CMS collaborations have also searched for exotic decays of the Higgs boson to long-lived neutral scalars ( $S$ ) in the Higgs-strahlung channel, for  $m_S < m_h/2$  [115,116]. The production process is  $pp \rightarrow ZH \rightarrow (Z \rightarrow \ell^+ \ell^-)(H \rightarrow SS \rightarrow b\bar{b}b\bar{b})$  [115] and  $pp \rightarrow ZH \rightarrow (Z \rightarrow \ell^+ \ell^-)(H \rightarrow SS \rightarrow 4j)$  [116]. We will mainly discuss the analysis strategy in Ref. [115] in the present discussion. Event selection requires the same flavor opposite sign lepton pair from  $Z$  boson and multijets from resonant Higgs decay. Reference [115] requires at least two tracks associated with the displaced vertex, and a lower bound is imposed on the reduced mass  $m/\Delta R_{\max} > 3$  GeV of the displaced vertex in order to veto the displaced vertices resulting from the random crossing of unrelated tracks. Here,  $m$  is the reconstructed invariant mass of the vertex ( $\sim m_S$ ), and  $\Delta R_{\max}$  is the maximum  $\Delta R$  separation between the track momentum and the combined momentum of other tracks associated with the displaced vertex. Within the parameter space of our interest, and considering the LLP signal process considered in our work,  $m$  could be roughly approximated to  $m_{\tilde{\chi}_2^0} - m_{\tilde{\chi}_1^0} \sim [25, m_Z]$  GeV, which overlaps with the region of  $m$  probed in Ref. [115]. However, for  $m_S$  much larger than  $2m_b$ , the tracks associated with the displaced vertex corresponding to  $S \rightarrow b\bar{b}$  decay would be collimated, leading to smaller  $\Delta R_{\max}$ . On the other hand,  $\Delta R_{\max}$  would be relatively larger when the long-lived candidate  $\tilde{\chi}_2^0$  undergoes three-body decay while also involving a missing particle, resulting in smaller reduced masses, which may not pass the selection cut considered in Ref. [115]. We note that the Ref. [115] excludes  $\sigma(pp \rightarrow ZH) \times \text{BR}(H \rightarrow SS)$  up to  $\sim 40$  fb at 95% C.L. at the  $\sqrt{s} = 13$  TeV LHC with  $\mathcal{L} = 139 \text{ fb}^{-1}$  from searches in the same flavor opposite sign dilepton plus at least two displaced  $b$  jets. A similar final state could be realized in the parameter space of our interest via the processes  $pp \rightarrow \tilde{\chi}_1^\pm \tilde{\chi}_3^0 / \tilde{\chi}_4^0 \rightarrow (\tilde{\chi}_1^\pm \rightarrow \tilde{\chi}_2^0 + W^\pm, \tilde{\chi}_2^0 \rightarrow \tilde{\chi}_1^0 + b\bar{b})(\tilde{\chi}_3^0 / \tilde{\chi}_4^0 \rightarrow \tilde{\chi}_2^0 + Z, \tilde{\chi}_2^0 \rightarrow \tilde{\chi}_1^0 + b\bar{b} / jj)$  with  $Z$  decaying via leptonic modes, and  $W$  decaying hadronically. For BP1, the production rate for  $pp \rightarrow \tilde{\chi}_1^\pm \tilde{\chi}_3^0 / \tilde{\chi}_4^0 \rightarrow (\tilde{\chi}_1^\pm \rightarrow \tilde{\chi}_2^0 + W^\pm)(\tilde{\chi}_3^0 / \tilde{\chi}_4^0 \rightarrow \tilde{\chi}_2^0 + Z)$  at  $\sqrt{s} = 13$  TeV is 0.616 fb, which is more than an order of magnitude smaller than the current upper limits in Refs. [115,116], thus escaping these constraints.

Searches have also been performed in multijet final states [117], which could arise from pair-produced gluinos or neutralinos in the  $R$ -parity violating SUSY scenario. The search in Ref. [117] triggers on high values of  $H_T$  ( $H_T > 1050$  GeV), where  $H_T$  is the scalar  $p_T$  sum of the

final state jets. The LLP signal realized within the parameter space of our interest comprises two  $\tilde{\chi}_1^0$  s, which results in missing energy signatures, with mass  $\gtrsim 100$  GeV. The  $H_T$  distribution for the LLP signal for our benchmark points typically peaks at lower values. Correspondingly, the signal efficiency in the signal region considered in Ref. [117] is smaller, leading to weaker constraints. The above discussion suggests the need for designing a strategy optimized for the final state of our interest. We will detail it in the following.

## E. Signal trigger and background

Before moving on to discuss the strategy to reconstruct the DSVs associated with  $\tilde{\chi}_2^0$ , let us examine the prompt components in the signal process. The  $WZ/WH_1$  pair produced through  $pp \rightarrow (\tilde{\chi}_1^\pm \rightarrow W^\pm \tilde{\chi}_2^0)(\tilde{\chi}_3^0 / \tilde{\chi}_4^0 \rightarrow Z/H_1 \tilde{\chi}_2^0)$  decay promptly and can lead to various different SM final states which could be triggered upon. In Fig. 10, we present the multiplicity  $n_\ell$  of isolated prompt leptons  $\ell$  ( $= e, \mu$ ) that can originate from the decay of  $WZ/WH_1$  pair in the signal process in Eq. (5.1) at truth level (red, dotted line) and detector level (solid blue line). At the detector level, an isolated lepton is required to satisfy

$$I(P) = \frac{\sum_{i \neq l} p_{T,i} \Delta R^{<0.3}}{p_{T,l}} < 0.1, \quad l = e, \mu, \quad (5.9)$$

where  $\sum_{i \neq l} p_{T,i} \Delta R^{<0.3}$  represents the sum of transverse momenta of all objects (excluding the lepton candidate) with  $p_T > 2$  GeV within a cone of radius  $\Delta R < 0.3$  centred around the candidate lepton,  $\Delta R = \sqrt{\Delta\eta^2 + \Delta\phi^2}$  where  $\Delta\eta$  and  $\Delta\phi$  are the pseudorapidity and azimuthal angle differences and  $p_{T,l}$  is the transverse momentum of the candidate lepton. We would like to note that these isolated leptons are also required to satisfy  $d_0 < 2$  mm.

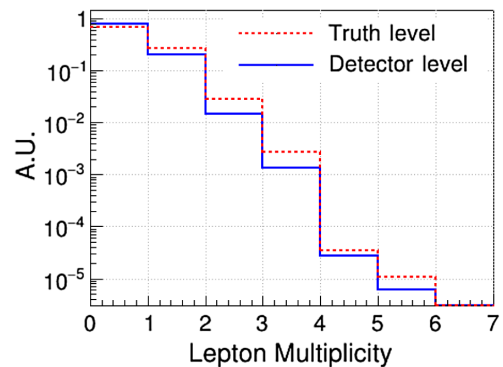


FIG. 10. Distribution for lepton multiplicity  $n_\ell$  ( $\ell = e, \mu$ ) from promptly decaying  $WZ/WH_1$  pair produced in the process  $pp \rightarrow (\tilde{\chi}_1^\pm \rightarrow W^\pm \tilde{\chi}_2^0)(\tilde{\chi}_3^0 / \tilde{\chi}_4^0 \rightarrow Z/H_1 \tilde{\chi}_2^0)$  at the HL-LHC. The truth level and detector level distributions are shown in solid red and solid blue, respectively.

The single prompt lepton final state in Fig. 10 can originate when the  $W$  decays leptonically,  $W \rightarrow \ell'\nu$  ( $\ell' = e, \mu, \tau$ ) while the  $Z/H_1$  decays hadronically. Similarly, the final state with two prompt leptons can arise when  $W$  decays hadronically ( $W \rightarrow jj$ ) while the  $Z/H_1$  decays via leptonic modes. The scenario with  $n_\ell = 3$  can arise when (1)  $W \rightarrow \ell'\nu, Z \rightarrow \ell'\ell'$ , (2)  $W \rightarrow \ell'\nu, H_1 \rightarrow \ell'\ell'$ , (3)  $W \rightarrow \ell'\nu, H_1 \rightarrow (W \rightarrow \ell'\nu)(W^* \rightarrow \ell'\nu)$ , (4)  $W \rightarrow \ell'\nu, H_1 \rightarrow (Z \rightarrow \ell'\ell')(Z^* \rightarrow jj)$  etc. Accordingly, we consider two different analysis categories corresponding to different signal triggers,  $n_\ell = 1$  and  $n_\ell = 2$ . The  $n_\ell = 3$  signal category is ignored due to smaller production rates relative to the other two. For  $n_\ell = 1$ , we require the isolated prompt lepton to satisfy  $p_{T,\ell} > 30$  GeV. Recall that the signal final state contains two long-lived  $\tilde{\chi}_2^0$  s. Therefore, in addition to prompt leptons, we will have displaced objects ( $b\bar{b}, \tau^\pm\tau^\mp, \ell^\pm\ell^\mp, j\bar{j}$ ) +  $\cancel{E}_T$ . The dominant backgrounds in this signal category are semileptonic  $t\bar{t}$  and  $W$  + jets. In the  $n_\ell = 2$  signal category, we impose  $p_{T,\ell_1} > 30$  GeV and  $p_{T,\ell_2} > 20$  GeV where  $p_{T,\ell_1} > p_{T,\ell_2}$ . The dominant backgrounds are dileptonic  $t\bar{t}$  and  $2\ell$  + jets, where *jets* mainly include  $b$  and  $c$  jets. We also require the isolated leptons to lie within  $|\eta| < 4.0$  and impose a lower threshold on the missing transverse energy  $\cancel{E}_T > 50$  GeV at the event selection stage. In principle, a stricter cut on the  $\cancel{E}_T$  can be imposed, the implications of which we have discussed later in Sec. V G. Alternatively, jet triggers can be used instead of lepton triggers since the  $WZ/WH_1$  pair in the signal can predominantly decay via hadronic modes. Choosing an optimized event triggering criteria for the online trigger systems viz. the L1 trigger and the HLT is among the most critical steps in any analysis (cf. Refs. [112,114] and references therein). The choice of efficient triggers is more pertinent for the L1 to ensure that the events of interest (viz. the LLPs in the present analysis) are not lost forever. The event selection rates at the HLT are, on average, an order of magnitude smaller than at the L1 system. Therefore, typically stronger thresholds are applied to the HLT system to ensure consistent event rates. In this regard, triggering on leptons is advantageous due to similar thresholds at the L1 trigger and the HLT, inclusiveness, and less susceptibility to pileup effects. For the case of a single isolated muon (electron), the values of L1 trigger seed of  $p_T > 22$  GeV (28 GeV) and  $|\eta| < 2.4$ , are pretty similar to the threshold at the HLT viz.  $p_T > 24$  GeV (32 GeV) [118,119]. On the other hand, HLT thresholds on  $p_T$  and the sum of transverse momenta  $H_T$  for the jet(s) are harder compared to their L1 counterparts. Therefore, jet-triggered events are vulnerable to considerable efficiency loss at the HLT. Furthermore, the jet thresholds are also strongly sensitive to the level of pileup, and the high pileup environment at the HL-LHC can degrade jet energy resolution leading to depleted trigger efficiencies [118]. Optimal jet trigger rates require the implementation of dedicated pileup mitigation techniques, which is beyond the scope of our work. Therefore, for

TABLE II. Summary of signal triggers and the basic selection cuts. These triggers are only applied to prompt objects. Tracks with  $|d_0| < 2$  mm are classified within the prompt category.

Signal triggers	
$ d_0  < 2$ mm	
$n_\ell = 1$	$n_\ell = 2$
$p_{T,\ell_1} > 30$ GeV	$p_{T,\ell_1} > 30$ GeV
	$p_{T,\ell_2} > 20$ GeV
	$\cancel{E}_T > 50$ GeV

simplicity, we adhere to lepton triggers only. The signal triggers and the corresponding selection cuts are summarized in Table II.

Besides the SM backgrounds, additional background contributions can arise from instrumental effects, such as hadronic interactions with the detector and misidentification or misreconstruction in tracking to produce high mass DSV with large track multiplicities. The instrumental background effects can be largely mitigated by imposing a lower threshold on the invariant mass of the tracks and requiring a high track multiplicity [110]. It is also worthwhile to note that it is rather challenging to simulate the instrumental background sources and can only be estimated through measured data. Hence, the inclusion of instrumental effects is beyond the scope of quasirealistic collider studies such as the present work. The only exception is the usage of signal regions for which the instrumental effects are estimated by the experimental collaborations. We adopt such a “realistic” signal region in addition to other “optimistic” signal regions (where instrumental background estimations are unavailable) in Sec. V G.

## F. Reconstructing the displaced secondary vertex from LLP $\tilde{\chi}_2^0$

As discussed earlier, the cascade decay channel for the directly produced  $\tilde{\chi}_3^0\tilde{\chi}_1^\pm/\tilde{\chi}_4^0\tilde{\chi}_1^\pm$  pair results into two  $\tilde{\chi}_2^0$  s in addition to other prompt SM candidates. The two LLP candidates can, in principle, lead to two displaced secondary vertices. In the signal, the tracks with larger transverse impact parameters are expected to originate from these two displaced secondary vertices. To reconstruct the final DSVs, we retrace the tracks with  $d_0 \geq 2$  mm.

In Fig. 11 (left), we present the distributions for  $d_0$  for the signal benchmarks BP1, BP2, and BP3. Here, we include all tracks with  $p_T > 1$  GeV and  $|\eta| < 4.0$  in events that pass the selection cuts corresponding to the signal trigger  $n_\ell = 1$ . The corresponding distributions for the dominant semileptonic  $t\bar{t}$  background are also illustrated in the same figure. We observe from Fig. 11 (left) that the tail of the distributions for the signal process shifts to larger  $|d_0|$  values with decreasing  $\Gamma_{\tilde{\chi}_2^0}$ . For BP3 the fraction of events ( $n_{\text{frac}}$ ) above  $|d_0| > 10$  cm,  $n_{\text{frac}} \sim 0.02$ . In this range of  $|d_0|$

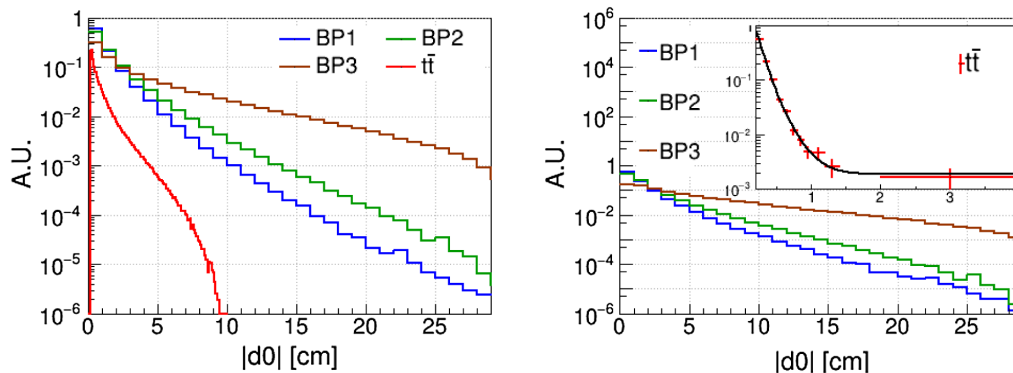


FIG. 11. Distribution of transverse impact parameter  $|d_0|$  for all tracks with  $p_T > 1$  GeV and  $|\eta| < 4$  corresponding to BP1 (blue), BP2 (green), and BP3 (brown), at the HL-LHC. Left panel: events pass the trigger choice  $n_\ell = 1$ . The corresponding distribution for the semileptonic  $t\bar{t}$  background is shown in red color. Right panel: events pass the trigger choice  $n_\ell = 1$  and have at least one displaced secondary vertex. The distribution for the semileptonic  $t\bar{t}$  background is shown in red color in the figure inset.

the fraction is considerably low for BP1 ( $n_{\text{frac}} \sim 0.001$ ) and BP2 ( $n_{\text{frac}} \sim 0.005$ ). Interestingly, the  $|d_0|$  distributions for the semileptonic  $t\bar{t}$  background extends all the way up to  $|d_0| \sim 10$  cm. This happens due to long-lived mesons like  $K_s^0$ ,  $\Lambda$ ,  $D$  etc. produced from  $b$  hadrons. Therefore, it is essential to explore other features of the LLP-specific topology which can reduce the backgrounds. One such entity that is largely exclusive to the phenomenology of long-lived decay is the displaced secondary vertex. As such, our next objective is to reconstruct the secondary vertices associated with the LLP  $\tilde{\chi}_2^0$ . We will also explore various observables that are contingent on the reconstructed DSVs, optimizing the selection cuts on them, and revisit the  $|d_0|$  distributions afterwards.

In an ideal scenario, tracks that arise from the same secondary vertex are expected to share a common point of origin  $\{x_0, y_0, z_0\}$ . Correspondingly, we allocate tracks with  $d_0 \geq 2$  mm whose point of origin are within  $\{|\Delta x| < 1$  mm,  $|\Delta y| < 1$  mm,  $|\Delta z| < 1$  mm $\}$  of each other, to a reconstructed vertex. Among them, the ones that contain at least three tracks are classified as a DSV. Having reconstructed the DSVs, let us revisit the distributions for  $|d_0|$ . We redraw the distributions for  $|d_0|$  in Fig. 11 (right), similar to that in Fig. 11 (left), except now with only those events which have at least one reconstructed DSV.

Let us also note the following important fact about the  $t\bar{t}$  background. Imposing the requirement for a reconstructed DSV leads to a major depletion in the  $d_0$  distributions for the semileptonic  $t\bar{t}$  background. It falls sharply before it reaches  $|d_0| \sim 2$  cm and suffers from substantial statistical uncertainty in the tail. Therefore, we extrapolate the shape of  $|d_0|$  for semileptonic  $t\bar{t}$  background using 5M  $t\bar{t}$  events in Fig. 11 (right) and is shown by the solid black line. To ensure consistency, we generate additional 6.5 M  $t\bar{t}$  events, and the extrapolated function derived in the previous step matches with the  $|d_0|$  distributions drawn for this new sample. Note that the long tail for the  $|d_0|$  distribution in

case of the  $t\bar{t}$  background is an artifact of rarity of events with large decay length in SM.

### G. LLP-specific observables at the detector level, cut flow, and signal significance

With an enhanced tracking algorithm, ATLAS shows a good reconstruction efficiency even for displaced tracks produced at a large radius within 30 cm from the primary interaction vertex [120]. In order to reconstruct a displaced vertex, first, the tracks from that vertex need to be successfully reconstructed. Tracks originating far from the center of the detector tend to have higher values of  $d_0$ . Standard track reconstruction has low efficiency for large  $d_0$  values. In the following, we construct a few variables without solely relying on  $d_0$  to eliminate the background.

We refer to DSVs with the highest and second highest track multiplicity as  $V_1$  and  $V_2$ , respectively. For illustration, we show the track multiplicity of  $V_1$ , referred to as  $N_{\text{trk}}^{V_1}$ , for BP1, BP2, and BP3, in Fig. 12 (upper left). These distributions are presented for the  $n_\ell = 1$  signal trigger region, summarized in Table II. We observe that  $N_{\text{trk}}^{V_1}$  can reach up to  $\sim 5$ – $6$  for a considerable fraction of signal events in all three benchmark points. On the other hand,  $N_{\text{trk}}^{V_1}$  reaches only up to  $\sim 3$  in the semileptonic  $t\bar{t}$  process, which is the dominant background when the signal trigger is  $n_\ell = 1$ . Accordingly, we optimize  $N_{\text{trk}}^{V_1}$  to improve signal-to-background discrimination. Another parameter of interest is  $r_{V_1}$ , which represents the radial distance of  $V_1$  from the PIV.  $r_{V_1}$  is computed as  $r_{V_1} = \sqrt{X_{V_1}^2 + Y_{V_1}^2 + Z_{V_1}^2}$ , where  $\{X_{V_1}, Y_{V_1}, Z_{V_1}\}$  are the coordinates of the reconstructed DSV  $V_1$  in a reference frame centered at PIV =  $\{0, 0, 0\}$ . In Fig. 12 (upper right), we illustrate  $r_{V_1}$  for the signal benchmarks and semileptonic  $t\bar{t}$  background, considering the  $n_\ell = 1$  signal trigger. The radial distance of the DSV from PIV is

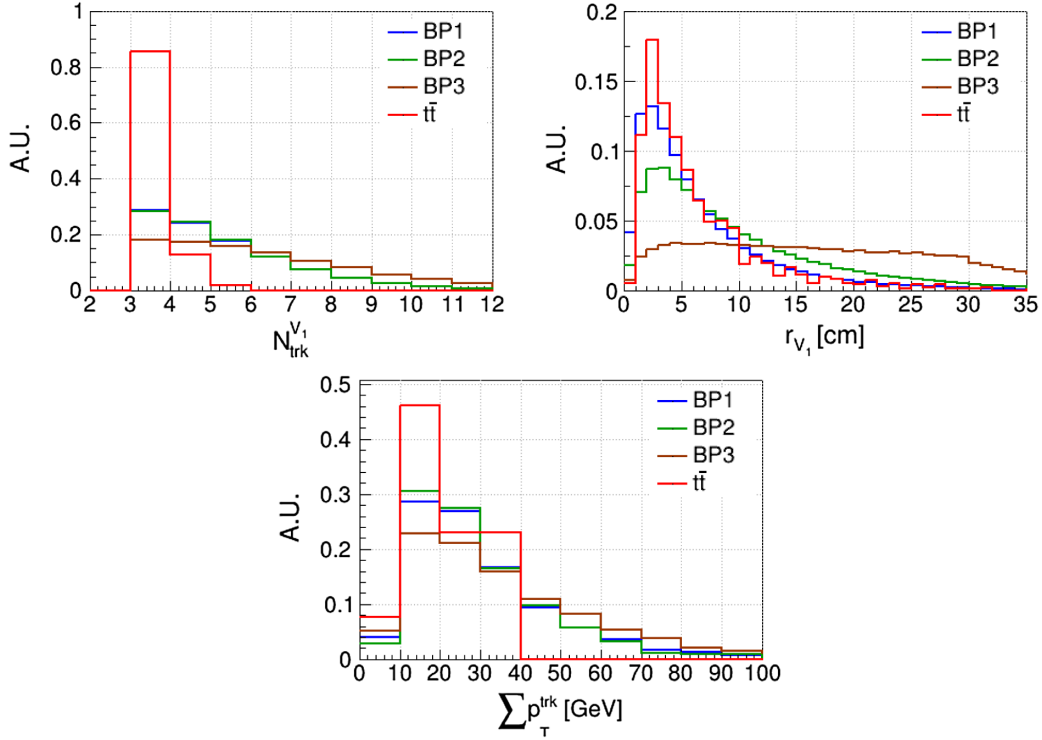


FIG. 12. Distributions for track multiplicity of DSV  $V_1$ ,  $N_{\text{trk}}^{V_1}$  (upper-left panel), radial distance of  $V_1$  from the primary interaction vertex,  $r_{V_1}$  (upper-right panel), and sum of transverse momentum of all tracks in  $V_1$ ,  $\sum p_T^{\text{trk}}$  (lower panel), in the  $pp \rightarrow \tilde{\chi}_1^\pm \tilde{\chi}_3^0 / \tilde{\chi}_4^0 \rightarrow (\tilde{\chi}_1^\pm \rightarrow \tilde{\chi}_2^0 + W^\pm, \tilde{\chi}_2^0 \rightarrow \tilde{\chi}_1^0 + Y)(\tilde{\chi}_3^0 / \tilde{\chi}_4^0 \rightarrow \tilde{\chi}_2^0 + Z/H_1, \tilde{\chi}_2^0 \rightarrow \tilde{\chi}_1^0 + Y)$  channel corresponding to BP1 (blue), BP2 (green), and BP3 (brown) at the HL-LHC. Here  $Y$  signifies all possible visible decay modes of  $\tilde{\chi}_2^0$ , as mentioned earlier. Distributions for the semileptonic  $t\bar{t}$  background are shown in red.

inversely proportional to the decay width of LLP in addition to the effect of Lorentz factor  $\beta\gamma$ . This behavior is illustrated in Fig. 12 (upper right) where the distributions for  $r_{V_1}$  get flattened, and the tail shifts to larger values as the decay length of  $\tilde{\chi}_2^0$  are increased. In the case of BP1, where  $\Gamma_{\tilde{\chi}_2^0} \sim 10^{-14}$  GeV,  $r_{V_1}$  peaks roughly at 2 cm. As we move to BP2, where  $\Gamma_{\tilde{\chi}_2^0}$  is smaller by an order of magnitude, the peak position shifts noticeably, however, the overall distributions get flatter. At further lower values of  $\Gamma_{\tilde{\chi}_2^0} \sim 10^{-16}$  GeV corresponding to BP3, we observe a considerable alteration in the distribution. The corresponding distribution for the semileptonic  $t\bar{t}$  background peaks at a much lower value  $r_{V_1} \sim 3$  cm. Overall, this observable demonstrates potential not only as a background discriminator but also as an excellent identifier of variations in the decay width of the LLP. Consequently, we optimize the selection cuts on  $r_{V_1}$  such that the signal significance  $S/\sqrt{B}$  is maximized, where  $S$  and  $B$  are the signal and background yields at the HL-LHC. In addition to  $N_{\text{trk}}^{V_1}$  and  $r_{V_1}$ , we also optimize the selection cut on the sum of transverse momentum of all tracks associated with  $V_1$ , represented as  $\sum p_T^{\text{trk}}$ . We present the distributions for  $\sum p_T^{\text{trk}}$  in Fig. 12 (bottom). The  $\sum p_T^{\text{trk}}$  distributions for both signal and

the  $t\bar{t}$  background peaks in the same region of 15 GeV, however, the background falls sharply compared to the signal. While the backgrounds become negligible at  $\sum p_T^{\text{trk}} \gtrsim 40$  GeV, the signal tail extends far beyond. Correspondingly, we optimize the upper limit on  $\sum p_T^{\text{trk}}$  in our cut-based analysis.

We first present the signal and background yields at the HL-LHC in the  $1\ell$  and  $2\ell$  signal categories in Table III, considering the selection cuts for the ‘‘Prompt sector’’ ( $|d_0| < 2$  mm) as discussed in Sec V E. The  $S/B$  ratio, where  $S$  and  $B$  are the signal and background yields at the HL-LHC, is  $\sim \mathcal{O}(10^{-6})$  after the application of prompt category cuts for all signal benchmarks and signal categories. Next, we discuss the implications of different DSV sensitive observables in the ‘‘Displaced sector’’ of the analysis where at least one DSV must be reconstructed. We have segregated this displaced sector into three broad regions based on  $|d_0|$ . The first signal region SR1 focuses on displaced tracks with  $|d_0| \geq 2$  mm. Two additional signal regions are considered where displaced objects are required to satisfy a more stringent  $|d_0|$  criteria viz  $|d_0| \geq 4$  mm (SR2) and  $|d_0| \geq 8$  mm (SR3).

It is worth noting that backgrounds from SM processes are negligible in the displaced vertex searches. It was shown by the LHC collaboration that in this type of analysis,

TABLE III. Selection cuts on lepton  $|d_0^{\ell}|$ ,  $|d_Z^{\ell}|$ ,  $p_T$  ( $i = 1, 2$ ) and  $\cancel{E}_T$  for prompt candidates are applied successively. These selection cuts tabulated under the prompt sector are common to all signal regions that are discussed later in each signal category. Signal and background rates are presented for  $\sqrt{s} = 14$  TeV LHC assuming  $\mathcal{L} = 3000 \text{ fb}^{-1}$ .

		Prompt sector ( $ d_0  < 2 \text{ mm}$ )		
		$ d_0^{\ell} ,  d_Z^{\ell}  < 2 \text{ mm}$	$p_T^{\ell_{1,2}} > 30, 20 \text{ GeV}$	$\cancel{E}_T > 50 \text{ GeV}$
$1\ell$	BP1	2590	2150	2088
	BP2	2004	1683	1638
	BP3	3646	3073	2975
	$t_{\text{ht}\ell}$	$2.4 \times 10^8$	$1.6 \times 10^8$	$1.15 \times 10^8$
$2\ell$	BP1	399	280	273
	BP2	300	215	210
	BP3	519	379	368
	$t_{\ell t\ell}$	$6.02 \times 10^7$	$4.5 \times 10^7$	$3.5 \times 10^7$

the background contribution is largely instrumental in nature [110,111]. We reiterate that the instrumental backgrounds can only be estimated from measured data. Hence, we first adopt a signal region defined in the ATLAS analysis [110,121] for which the instrumental background has been estimated. We refer to this ‘‘realistic’’ signal region as  $\text{SR}_A$ . It considers displaced charged tracks with  $|d_0| \geq 4 \text{ mm}$ , requires at least one DSV with  $N_{\text{trk}} \geq 5$  and the invariant mass of the tracks associated with the DSV must be greater than  $m_{\text{trk}} > 10 \text{ GeV}$ . A considerable fraction of events for our signal benchmarks can pass these thresholds, as shown in Fig. 13, where we display the number of signal

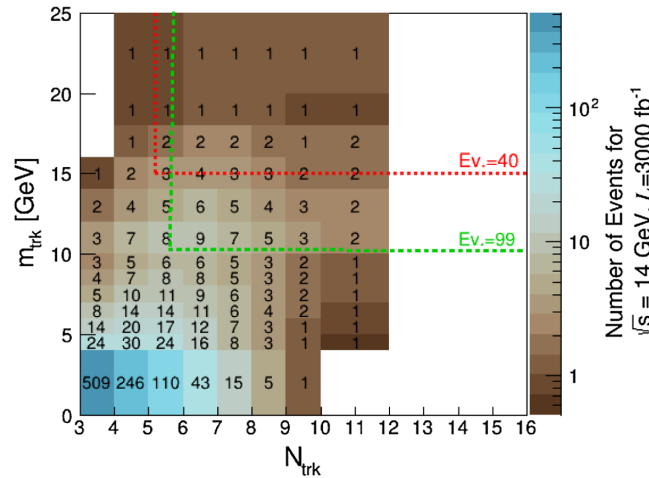


FIG. 13. Number of signal events at the HL-LHC for the representative benchmark BP1 as a function of the invariant mass of the tracks  $m_{\text{trk}}$  and the number of tracks  $N_{\text{trk}}$  for at least one displaced secondary vertex with  $|d_0| \geq 4 \text{ mm}$ . The green and red dotted line corresponds to the boundary of  $|d_0| \geq 4 \text{ mm}$ ,  $N_{\text{trk}} \geq 5$  signal region with  $m_{\text{trk}} > 10$  and  $15 \text{ GeV}$ , respectively. The signal yield for both regions is shown for HL-LHC.

TABLE IV. Signal rates for region  $\text{SR}_A$  at HL-LHC are presented. The background is estimated from instrumental effect for this signal region from ATLAS analysis [121]. Signal significance corresponding to three times this background is estimated.

	BP1	BP2	BP3
$m_{\geq 5\text{trk}} > 10 \text{ GeV}$ , $N_{\text{trk}} \geq 5$ ( $\mathcal{L} = 3 \text{ ab}^{-1}$ )	99	70	422
SM Background	...	...	...
Instrumental Background ( $\mathcal{L} = 139 \text{ fb}^{-1}$ )	5	5	5
$\frac{S}{\sqrt{B}}$ ( $3 \times \text{Ins BG}$ , $\mathcal{L} = 3 \text{ fb}^{-1}$ )	5.5	3.9	23

events for BP1 at the HL-LHC as a function of  $m_{\text{trk}}$  and  $N_{\text{trk}}$ . We notice from Fig. 13 that  $\sim 99$  signal events pass the selection cuts mentioned above at the HL-LHC for BP1. The ATLAS collaboration has estimated the instrumental background rate for  $\text{SR}_A$  to be  $\sim 5$  at the  $\sqrt{s} = 13 \text{ TeV}$  LHC with  $\mathcal{L} \sim 139 \text{ fb}^{-1}$  [121]. We extrapolate the background estimate  $B$  to the HL-LHC through the luminosity scaling and triple the background estimates further to incorporate the effects of high pileup at the HL-LHC,  $B \sim 5 \times (3000/139) \times 3.0 \sim 324$ . We have shown the signal significance computed as  $S/\sqrt{B}$  in Table IV for the three benchmark points. With this background estimation, the signal significance for BP1, BP2, and BP3, turns out to be  $\sim 5.5$ ,  $3.9$ , and  $23\sigma$ , respectively. Thus, our results indicate that it should be possible to probe the LLP signature from the representative benchmark point BP1 and BP3 at the HL-LHC even after folding in considerations of instrumental backgrounds.

While  $\text{SR}_A$  considers displaced tracks with  $|d_0| > 4 \text{ mm}$ , it is worth exploring other signal regions with different choices for  $|d_0|$ . For example, the CMS analysis in Ref. [122] considers signal regions with  $|d_0| > 2 \text{ mm}$ . In this regard, we consider three different signal regions  $\text{SR}_1$ ,  $\text{SR}_2$ , and  $\text{SR}_3$  with  $|d_0| > 2 \text{ mm}$ ,  $|d_0| > 4 \text{ mm}$ , and  $|d_0| > 8 \text{ mm}$ , respectively, with optimized selection cuts on  $N_{\text{trk}}^{V_1}$ ,  $\sum p_T^{\text{trk}}$ ,  $r_{V_1}$ , and  $N_{\text{trk}}^{V_2}$  (number of tracks from vertex  $V_2$ ). We present the optimized selection cuts in the displaced sector for  $\text{SR}_1$ ,  $\text{SR}_2$ , and  $\text{SR}_3$  for the  $n_{\ell} = 1(2)$  signal category in Table V. The event rates at the HL-LHC for the three signal benchmarks (BP1, BP2, BP3) and the dominant  $t\bar{t}$  background are also shown.

We observe from Table V that the requirement for at least one DSV with  $N_{\text{trk}}^{V_1} \geq 3$  using displaced tracks with  $|d_0| > 2 \text{ mm}$  improves  $S/B$  from  $\sim \mathcal{O}(10^{-6})$  (after imposing selection cuts from the prompt sector) to  $\sim \mathcal{O}(10^{-3})$ . Furthermore, this requirement leads to negligible event rates for  $W + \text{jets}$  and  $Z + \text{jets}$  in both  $n_{\ell} = 1$  and  $n_{\ell} = 2$  signal categories, respectively. In this light, we ignore these backgrounds in our analysis. The subsequent imposition of  $N_{\text{trk}}^{V_1} \geq 5$  in  $\text{SR}_1$  reduces the SM background rates further by a factor of  $\sim 50$  while the signal rates for the three

TABLE V. Selection cuts on the displaced candidates and the cut flow for SR1, SR2, and SR3 are shown. The selection cuts shown here have been applied in succession to the selection cuts on the prompt candidates shown in Table III. We note that the instrumental background estimates are unavailable for SR1–3.

		SR1 $ d_0  \geq 2$ mm				SR2 $ d_0  \geq 4$ mm		SR3 $ d_0  \geq 8$ mm		
		$N_{\text{trk}}^{V1} \geq 3$	$N_{\text{trk}}^{V1} \geq 5$	$\sum p_T^{\text{trk}} < 30$ GeV	$r_{V_1} \geq 4$ cm	$N_{\text{trk}}^{V2} \geq 5$	$N_{\text{trk}}^{V1} \geq 3$	$N_{\text{trk}}^{V1} \geq 5$	$N_{\text{trk}}^{V1} \geq 3$	$N_{\text{trk}}^{V1} \geq 5$
$1\ell$	$t_h t_e$	109453	1937	1210	484	0	2422	0	242	0
	BP1	1348	635	428	226	27	1087	459	741	271
	BP2	1204	569	389	272	38	1047	447	809	301
	BP3	1198	770	430	390	40	1154	723	1078	648
$2\ell$	$t_e t_e$	35712	624	406	281	0	812	0	62	0
	BP1	174	82	55	30	4	140	59	96	35
	BP2	152	71	49	35	5	132	56	102	38
	BP3	147	93	52	47	5	142	87	132	78

TABLE VI. Signal and background rates are presented for  $\sqrt{s} = 14$  TeV LHC assuming  $\mathcal{L} = 3000$  fb $^{-1}$  for the selection cuts corresponding to signal region SR1 (Table V) except for a stronger lower bound on missing transverse energy  $\cancel{E}_T > 120$  GeV.

		Prompt sector $ d_0  < 2$ mm			SR1 $ d_0  \geq 2$ mm				
		$D_0^\ell, D_Z^\ell < 2$ mm	$p_T^\ell > 30$ GeV	$\cancel{E}_T > 120$ GeV	$N_{\text{trk}}^{V1} \geq 3$	$N_{\text{trk}}^{V1} \geq 5$	$\sum p_T^{\text{trk}} < 30$ GeV	$r_{V_1} \geq 4$ cm	$N_{\text{trk}}^{V2} \geq 5$
$1\ell$	BP1	2590	2150	1837	1183	557	377	198	23
	BP2	2003	1683	1456	1068	504	346	242	33
	BP3	3646	3073	2561	1021	655	368	333	33
	$t_h t_e$	$2.4 \times 10^8$	$1.6 \times 10^8$	$1.9 \times 10^7$	14771	726	484	242	0

benchmarks reduces only by a factor of  $\sim 2$ . For SR1, the SM background further reduces to negligible values on imposing  $\sum p_T^{\text{trk}} < 30$  GeV,  $r_{V_1} \geq 4$  cm, and  $N_{\text{trk}}^{V2} \geq 5$  in both the  $n_\ell = 1$  and  $n_\ell = 2$  signal categories. For SR2 and SR3, the SM backgrounds are suppressed on applying  $N_{\text{trk}}^{V1} \geq 5$ . However, the results presented in Table V are rather conservative estimates since the instrumental background rates are unavailable for SR1–3 and, therefore, could not be considered. While it is true that the instrumental backgrounds, which are not available for SR1, SR2, and SR3, might imply that we overestimate the efficacy of our analysis to remove the background events entirely, it is worth noting that one gets encouraging values for significance at the last but one step in the analysis where the SM background is not yet completely absent. For example, for BP3 in  $1\ell$  channel for the signal regions [SR1, SR2, SR3], these significance values are [17.7, 23.4, 69]  $\sigma$ . Similarly, for  $2\ell$  channel, the  $\sigma_s$ s for BP3 in the three signal regions are 2.8, 5.0, and 16.8 $\sigma$ . Hence SR1–3 show promising prospects to further perform a realistic collider analysis with instrumental backgrounds.

Another area of optimization can be the  $\cancel{E}_T$  selection criteria. In SR1, we imposed  $\cancel{E}_T > 50$  GeV as baseline selection. We performed a similar analysis with a stronger lower bound on  $\cancel{E}_T$ . The HL-LHC rates are shown in

Table VI for the  $1\ell$  channel in SR1 with  $\cancel{E}_T > 120$  GeV. This stronger  $\cancel{E}_T$  cut reduces the background in the prompt sector by almost an order of magnitude, while the signal reduces roughly by 10% when compared with the yields of Table V. This leads to improved signal-vs.-background ratios at successive stages of the analysis. However, in both cases, the kinematic variables for the displaced vertex completely remove the SM background. It is worth noting that we considered a weaker cut on  $\cancel{E}_T$  ( $\cancel{E}_T > 50$  GeV) in SR1 to emphasize the relevance of observables related to the DSV. Our goal was to highlight that despite a weaker selection cut on  $\cancel{E}_T$ , the variables associated with the reconstructed displaced vertex efficiently reduce the SM background.

## VI. OUTLOOK AND CONCLUSION

In this work, we focus on the case of singlinolike light neutralino DM in the NMSSM framework. Implications from current collider and astrophysical constraints have been analyzed, and the allowed parameter space has been scrutinized in light of projected sensitivities in the future direct detection experiments. We consider an electroweakino mass spectrum where  $\tilde{\chi}_2^0$  has a dominant bino admixture,  $\tilde{\chi}_3^0, \tilde{\chi}_4^0, \tilde{\chi}_1^\pm$  have a dominant Higgsino

composition, and  $\tilde{\chi}_5^0, \tilde{\chi}_2^\pm$  are winolike. In the allowed region of parameter space, there exists long-lived binolike NLSP  $\tilde{\chi}_2^0$ . The small decay width of this  $\tilde{\chi}_2^0$  being caused for,  $\Delta M = m_{\tilde{\chi}_2^0} - m_{\tilde{\chi}_1^0} < m_Z$  which allows only three-body decay for  $\tilde{\chi}_2^0$ . Within the scope of the allowed parameter space of interest, the long-lived  $\tilde{\chi}_2^0$  can decay through  $\tilde{\chi}_2^0 \rightarrow \tilde{\chi}_1^0 b \bar{b}$ ,  $\tilde{\chi}_2^0 \rightarrow \tilde{\chi}_1^0 \tau^+ \tau^-$ ,  $\tilde{\chi}_2^0 \rightarrow l^+ l^-$ ,  $\tilde{\chi}_2^0 \rightarrow \tilde{\chi}_1^0 j \bar{j}$ , or  $\tilde{\chi}_2^0 \rightarrow \tilde{\chi}_1^0 \gamma$ . The  $\tilde{\chi}_2^0$ s can appear in direct electroweakino searches at the LHC via cascade decays of heavier electroweakinos, and lead to displaced secondary vertices, which can be reconstructed in the tracker region of the LHC. In this work, we study the projected sensitivity for direct electroweakino production  $pp \rightarrow \tilde{\chi}_3^0 / \tilde{\chi}_4^0 \tilde{\chi}_1^\pm \rightarrow (\tilde{\chi}_3^0 / \tilde{\chi}_4^0 \rightarrow Z / H, \tilde{\chi}_2^0) (\tilde{\chi}_1^\pm \rightarrow W^\pm \tilde{\chi}_2^0)$  with  $\tilde{\chi}_2^0 \rightarrow \tilde{\chi}_1^0 Y$  at the HL-LHC. We choose three different signal benchmarks BP1, BP2, and BP3, from the currently allowed parameter space that features a long-lived  $\tilde{\chi}_2^0$ . We perform a detailed collider analysis using the cut-and-count methodology while including signal and relevant backgrounds at the detector level.

We consider two different signal categories,  $n_\ell = 1, 2$  as discussed in Sec. V. To separate the signal from the background effectively, we use selection cuts on separate sets of observables in case of prompt and long-lived objects. Objects with transverse impact parameter  $|d_0| < 2$  mm are classified as prompt, while those with  $|d_0| \geq 2$  mm are categorized as long lived. Prompt objects are used to trigger the events, while the displaced objects play the major role in discriminating against the backgrounds. We identify the signal regions SR1 with optimized selection cuts on  $N_{\text{trk}}^{V_1}$ , the track multiplicity of  $V_1$ ,  $\sum p_T^{\text{trk}}$ , sum of transverse momentum of all tracks associated with  $V_1$ ,  $r_{V_1}$ , radial distance between  $V_1$  and PIV, and  $N_{\text{trk}}^{V_2}$ , track multiplicity for the second DSV. SR2 and SR3 are defined by optimizing the cuts on  $|d_0|$ , the minimum transverse impact parameter, and  $N_{\text{trk}}^{V_1}$ . We show that with the choice of

the three signal regions, SR1, SR2, and SR3, one can completely suppress the SM background. However, considering a purely instrumental background for the signal region  $\text{SR}_A$  as estimated in Ref. [121], scaling it to the HL-LHC luminosity and additionally tripling this scaled background to account for the effect of difficulties of the HL-LHC environment, we found that BP1, BP2, and BP3 can be probed with a signal significance of  $\sigma_S \gtrsim 5.5, 3.9$ , and  $23\sigma$  in  $\text{SR}_A$  (cf. Table IV). Similar analysis can be extended to other points in the allowed parameter space of our interest to evaluate their exclusion/discovery at the high luminosity LHC.

## ACKNOWLEDGMENTS

A. A. acknowledges partial financial support from the Polish National Science Center under the Beethoven series Grant No. 2016/23/G/ST2/04301. In the final stage of this project, the research of A. A. has received funding from the Norwegian Financial Mechanism for years 2014–2021, Grant No. DEC-2019/34/H/ST2/00707. R. K. B. thanks the U.S. Department of Energy for the financial support, under Grant No. DE-SC0016013. Some computing for this project was performed at the High Performance Computing Center at Oklahoma State University, supported in part by the National Science Foundation Grant OAC-1531128. R. K. B. thanks Rhitaja Sengupta for helpful discussions. S. K. is supported by Austrian Science Fund Elise Richter Fellowship V592-N27 and research group funding FG1. We acknowledge Austrian-India Wissenschaftlich-Technische Zusammenarbeit (WTZ) and Department of Atomic Energy (DAE) exchange Project No. IN 15/2018. R. G. wishes to thank the Indian National Science Academy for support under the INSA senior scientist scheme. A. D. would like to acknowledge the support of Innovation in Science Pursuit for Inspired Research (INSPIRE) Fellowship IF160414.

- 
- [1] N. Aghanim *et al.*, Planck 2018 results. VI. Cosmological parameters, *Astron. Astrophys.* **641**, A6 (2020); **652**, C4 (E) (2021).
  - [2] M. Tanabashi *et al.*, Review of particle physics, *Phys. Rev. D* **98**, 030001 (2018).
  - [3] Eldad Gildener and Steven Weinberg, Symmetry breaking and scalar bosons, *Phys. Rev. D* **13**, 3333 (1976).
  - [4] Leonard Susskind, Dynamics of spontaneous symmetry breaking in the Weinberg-Salam theory, *Phys. Rev. D* **20**, 2619 (1979).
  - [5] Gerard 't Hooft, Naturalness, chiral symmetry, and spontaneous chiral symmetry breaking, *NATO Sci. Ser. B* **59**, 135 (1980).
  - [6] J. Wess and B. Zumino, Supergauge transformations in four dimensions, *Nucl. Phys.* **B70**, 39 (1974).
  - [7] H. P. Nilles, Supersymmetry, supergravity and particle physics, *Phys. Rep.* **110**, 1 (1984).
  - [8] H. E. Haber and G. L. Kane, The search for supersymmetry: Probing physics beyond the standard model, *Phys. Rep.* **117**, 75 (1985).
  - [9] Manuel Drees, Rohini Godbole, and Probir Roy, *Theory and Phenomenology of Sparticles* (World Scientific, Singapore, 2005), 10.1142/4001.
  - [10] Howard Baer and Xerxes Tata, *Weak Scale Supersymmetry: From Superfields to Scattering Events* (Cambridge University Press, Cambridge, England, 2006), 10.1017/CBO9780511617270.

- [11] Gianfranco Bertone, Dan Hooper, and Joseph Silk, Particle dark matter: Evidence, candidates and constraints, *Phys. Rep.* **405**, 279 (2005).
- [12] G. Belanger, Dark matter and the LHC, *Nucl. Phys. B, Proc. Suppl.* **194**, 5 (2009).
- [13] Rahool Kumar Barman, Genevieve Belanger, and Rohini M. Godbole, Status of low mass LSP in SUSY, *Eur. Phys. J. Spec. Top.* **229**, 3159 (2020).
- [14] Benjamin W. Lee and Steven Weinberg, Cosmological Lower Bound on Heavy-Neutrino Masses, *Phys. Rev. Lett.* **39**, 165 (1977).
- [15] Takeo Moroi and Lisa Randall, Wino cold dark matter from anomaly mediated SUSY breaking, *Nucl. Phys.* **B570**, 455 (2000).
- [16] Katherine Garrett and Gintaras Duda, Dark matter: A primer, *Adv. Astron.* **2011**, 968283 (2011).
- [17] Steven Weinberg, Cosmological Constraints on the Scale of Supersymmetry Breaking, *Phys. Rev. Lett.* **48**, 1303 (1982).
- [18] John Ellis, D. V. Nanopoulos, and Subir Sarkar, The cosmology of decaying gravitinos, *Nucl. Phys.* **B259**, 175 (1985).
- [19] Graciela B. Gelmini and Paolo Gondolo, Neutralino with the right cold dark matter abundance in (almost) any supersymmetric model, *Phys. Rev. D* **74**, 023510 (2006).
- [20] Howard Baer, Ki-Young Choi, Jihn E. Kim, and Leszek Roszkowski, Dark matter production in the early Universe: Beyond the thermal WIMP paradigm, *Phys. Rep.* **555**, 1 (2015).
- [21] Luis Aparicio, Michele Cicoli, Bhaskar Dutta, Sven Krippendorf, Anshuman Maharana, Francesco Muia, and Fernando Quevedo, Non-thermal CMSSM with a 125 GeV Higgs, *J. High Energy Phys.* **05** (2015) 098.
- [22] Luis Aparicio, Michele Cicoli, Bhaskar Dutta, Francesco Muia, and Fernando Quevedo, Light higgsino dark matter from non-thermal cosmology, *J. High Energy Phys.* **11** (2016) 038.
- [23] Leszek Roszkowski, Sebastian Trojanowski, and Krzysztof Turzynski, Towards understanding thermal history of the Universe through direct and indirect detection of dark matter, *J. Cosmol. Astropart. Phys.* **10** (2017) 005.
- [24] Rahool Kumar Barman, Genevieve Belanger, Biplob Bhattacharjee, Rohini Godbole, Gaurav Mendiratta, and Dipan Sengupta, Invisible decay of the Higgs boson in the context of a thermal and nonthermal relic in MSSM, *Phys. Rev. D* **95**, 095018 (2017).
- [25] Toby Falk, Keith A. Olive, and Mark Srednicki, Heavy sneutrinos as dark matter, *Phys. Lett. B* **339**, 248 (1994).
- [26] Armen Tumasyan *et al.*, Search for chargino-neutralino production in events with Higgs and W bosons using  $137 \text{ fb}^{-1}$  of proton-proton collisions at  $\sqrt{s} = 13 \text{ TeV}$ , *J. High Energy Phys.* **10** (2021) 045.
- [27] G. Aad *et al.* (ATLAS Collaboration), Search for charginos and neutralinos in final states with two boosted hadronically decaying bosons and missing transverse momentum in  $pp$  collisions at  $\sqrt{s} = 13 \text{ TeV}$  with the atlas detector, *Phys. Rev. D* **104**, 112010 (2021).
- [28] Lorenzo Calibbi, Jonas M. Lindert, Toshihiko Ota, and Yasutaka Takanishi, Cornering light neutralino dark matter at the LHC, *J. High Energy Phys.* **10** (2013) 132.
- [29] Genevieve Bélanger, Guillaume Drieu La Rochelle, Béranger Dumont, Rohini M. Godbole, Sabine Kraml, and Suchita Kulkarni, LHC constraints on light neutralino dark matter in the MSSM, *Phys. Lett. B* **726**, 773 (2013).
- [30] M. Cahill-Rowley, J. L. Hewett, A. Ismail, and T. G. Rizzo, Lessons and prospects from the pMSSM after LHC run I, *Phys. Rev. D* **91**, 055002 (2015).
- [31] Junjie Cao, Yangle He, Liangliang Shang, Wei Su, and Yang Zhang, Testing the light dark matter scenario of the MSSM at the LHC, *J. High Energy Phys.* **03** (2016) 207.
- [32] N. Arkani-Hamed, A. Delgado, and G. F. Giudice, The Well-tempered neutralino, *Nucl. Phys.* **B741**, 108 (2006).
- [33] Howard Baer, Vernon Barger, and Hasan Serce, SUSY under siege from direct and indirect WIMP detection experiments, *Phys. Rev. D* **94**, 115019 (2016).
- [34] Manimala Chakraborti, Utpal Chattopadhyay, and Sujoy Poddar, How light a higgsino or a wino dark matter can become in a compressed scenario of MSSM, *J. High Energy Phys.* **09** (2017) 064.
- [35] Jihn E. Kim and Hans Peter Nilles, The  $\mu$  problem and the strong  $CP$  problem, *Phys. Lett.* **138B**, 150 (1984).
- [36] H. P. Nilles, M. Srednicki, and D. Wyler, Weak interaction breakdown induced by supergravity, *Phys. Lett.* **120B**, 346 (1983).
- [37] J. Ellis, J. F. Gunion, H. E. Haber, L. Roszkowski, and F. Zwirner, Higgs bosons in a nonminimal supersymmetric model, *Phys. Rev. D* **39**, 844 (1989).
- [38] Ulrich Ellwanger, Michel Rausch de Traubenberg, and Carlos A. Savoy, Particle spectrum in supersymmetric models with a gauge singlet, *Phys. Lett. B* **315**, 331 (1993).
- [39] S. A. Abel, Subir Sarkar, and I. B. Whittingham, Neutralino dark matter in a class of unified theories, *Nucl. Phys.* **B392**, 83 (1993).
- [40] Jonathan Kozaczuk and Stefano Profumo, Light NMSSM neutralino dark matter in the wake of CDMS II and a 126 GeV Higgs boson, *Phys. Rev. D* **89**, 095012 (2014).
- [41] Junjie Cao, Chengcheng Han, Lei Wu, Peiwen Wu, and Jin Min Yang, A light SUSY dark matter after CDMS-II, LUX and LHC Higgs data, *J. High Energy Phys.* **05** (2014) 056.
- [42] Tao Han, Zhen Liu, and Shufang Su, Light neutralino dark matter: Direct/indirect detection and collider searches, *J. High Energy Phys.* **08** (2014) 093.
- [43] Ulrich Ellwanger and Cyril Hugonie, The semi-constrained NMSSM satisfying bounds from the LHC, LUX and Planck, *J. High Energy Phys.* **08** (2014) 046.
- [44] Junjie Cao, Demin Li, Jingwei Lian, Yuanfang Yue, and Haijing Zhou, Singlino-dominated dark matter in general NMSSM, *J. High Energy Phys.* **06** (2021) 176.
- [45] Haijing Zhou, Junjie Cao, Jingwei Lian, and Di Zhang, Singlino-dominated dark matter in  $Z_3$ -symmetric NMSSM, *Phys. Rev. D* **104**, 015017 (2021).
- [46] Rahool Kumar Barman, Genevieve Bélanger, Biplob Bhattacharjee, Rohini Godbole, Dipan Sengupta, and Xerxes Tata, Current bounds and future prospects of light neutralino dark matter in NMSSM, *Phys. Rev. D* **103**, 015029 (2021).
- [47] Monoranjan Guchait and Arnab Roy, Light singlino dark matter at the LHC, *Phys. Rev. D* **102**, 075023 (2020).
- [48] Haiying Cai, Hsin-Chia Cheng, and John Terning, A quirky little Higgs model, *J. High Energy Phys.* **05** (2009) 045.

- [49] Z. Chacko, Hock-Seng Goh, and Roni Harnik, The Twin Higgs: Natural Electroweak Breaking from Mirror Symmetry, *Phys. Rev. Lett.* **96**, 231802 (2006).
- [50] Matthew Baumgart, Clifford Cheung, Joshua T. Ruderman, Lian-Tao Wang, and Itay Yavin, Non-Abelian dark sectors and their collider signatures, *J. High Energy Phys.* **04** (2009) 014.
- [51] David E. Kaplan, Markus A. Luty, and Kathryn M. Zurek, Asymmetric dark matter, *Phys. Rev. D* **79**, 115016 (2009).
- [52] Keith R. Dienes and Brooks Thomas, Dynamical dark matter: I. Theoretical overview, *Phys. Rev. D* **85**, 083523 (2012).
- [53] Keith R. Dienes, Shufang Su, and Brooks Thomas, Distinguishing dynamical dark matter at the LHC, *Phys. Rev. D* **86**, 054008 (2012).
- [54] Juliette Alimena *et al.*, Searching for long-lived particles beyond the standard model at the large hadron collider, *J. Phys. G* **47**, 090501 (2020).
- [55] R. Barbier *et al.*, R-parity violating supersymmetry, *Phys. Rep.* **420**, 1 (2005).
- [56] Savas Dimopoulos, Michael Dine, Stuart Raby, and Scott D. Thomas, Experimental Signatures of Low-Energy Gauge Mediated Supersymmetry Breaking, *Phys. Rev. Lett.* **76**, 3494 (1996).
- [57] G. F. Giudice and R. Rattazzi, Theories with gauge mediated supersymmetry breaking, *Phys. Rep.* **322**, 419 (1999).
- [58] Jonathan L. Feng, Takeo Moroi, Lisa Randall, Matthew Strassler, and Shu-fang Su, Discovering Supersymmetry at the Tevatron in Wino LSP Scenarios, *Phys. Rev. Lett.* **83**, 1731 (1999).
- [59] Ulrich Ellwanger, Cyril Hugonie, and Ana M. Teixeira, The next-to-minimal supersymmetric standard model, *Phys. Rep.* **496**, 1 (2010).
- [60] Ulrich Ellwanger, Cyril Hugonie, and Ana M. Teixeira, The next-to-minimal supersymmetric standard model, *Phys. Rep.* **496**, 1 (2010).
- [61] Sebastian Baum, Katherine Freese, Nausheen R. Shah, and Bibhushan Shakya, NMSSM Higgs boson search strategies at the LHC and the mono-Higgs signature in particular, *Phys. Rev. D* **95**, 115036 (2017).
- [62] Marcela Carena, Howard E. Haber, Ian Low, Nausheen R. Shah, and Carlos E. M. Wagner, Alignment limit of the NMSSM Higgs sector, *Phys. Rev. D* **93**, 035013 (2016).
- [63] Ji Ji Fan and Matthew Reece, In vino veritas? Indirect searches shed light on neutralino dark matter, *J. High Energy Phys.* **10** (2013) 124.
- [64] Joseph Bramante, Nishita Desai, Patrick Fox, Adam Martin, Bryan Ostdiek, and Tilman Plehn, Towards the final word on neutralino dark matter, *Phys. Rev. D* **93**, 063525 (2016).
- [65] Alexander Kusenko, Paul Langacker, and Gino Segre, Phase transitions and vacuum tunneling into charge and color breaking minima in the MSSM, *Phys. Rev. D* **54**, 5824 (1996).
- [66] Debtosh Chowdhury, Rohini M. Godbole, Kirtimaan A. Mohan, and Sudhir K. Vempati, Charge and color breaking constraints in MSSM after the Higgs discovery at LHC, *J. High Energy Phys.* **02** (2014) 110; **03** (2018) 149(E).
- [67] Marcela Carena, H. E. Haber, S. Heinemeyer, W. Hollik, C. E. M. Wagner, and G. Weiglein, Reconciling the two loop diagrammatic and effective field theory computations of the mass of the lightest CP—even Higgs boson in the MSSM, *Nucl. Phys.* **B580**, 29 (2000).
- [68] Felix Brummer, Sabine Kraml, and Suchita Kulkarni, Anatomy of maximal stop mixing in the MSSM, *J. High Energy Phys.* **08** (2012) 089.
- [69] Ulrich Ellwanger, John F. Gunion, and Cyril Hugonie, Nmhdecay: A fortran code for the Higgs masses, couplings and decay widths in the NMSSM, *J. High Energy Phys.* **02** (2005) 066.
- [70] Ulrich Ellwanger and Cyril Hugonie, Nmhdecay 2.1: An updated program for sparticle masses, Higgs masses, couplings and decay widths in the NMSSM, *Comput. Phys. Commun.* **175**, 290 (2006).
- [71] Georges Aad *et al.*, Combined Measurement of the Higgs Boson Mass in  $pp$  Collisions at  $\sqrt{s} = 7$  and 8 TeV with the ATLAS and CMS Experiments, *Phys. Rev. Lett.* **114**, 191803 (2015).
- [72] B. C. Allanach, A. Djouadi, J. L. Kneur, W. Porod, and P. Slavich, Precise determination of the neutral Higgs boson masses in the MSSM, *J. High Energy Phys.* **09** (2004) 044.
- [73] S. Heinemeyer, W. Hollik, H. Rzehak, and G. Weiglein, The Higgs sector of the complex MSSM at two-loop order: QCD contributions, *Phys. Lett. B* **652**, 300 (2007).
- [74] S. Borowka, T. Hahn, S. Heinemeyer, G. Heinrich, and W. Hollik, Renormalization scheme dependence of the two-loop QCD corrections to the neutral Higgs-boson masses in the MSSM, *Eur. Phys. J. C* **75**, 424 (2015).
- [75] Delphi L3 LEPSUSYWG, Aleph and OPAL experiment note LEPSUSYWG/01-03.1, Combined LEP chargino mass limits, <http://lepsusy.web.cern.ch/lepsusy>.
- [76] G. Abbiendi *et al.*, Search for chargino and neutralino production at  $\sqrt{s} = 192$ -GeV to 209 GeV at LEP, *Eur. Phys. J. C* **35**, 1 (2004).
- [77] S. Schael *et al.*, Precision electroweak measurements on the Z resonance, *Phys. Rep.* **427**, 257 (2006).
- [78] Albert M Sirunyan *et al.*, Measurements of Higgs boson production cross sections and couplings in the diphoton decay channel at  $\sqrt{s} = 13$  TeV, *J. High Energy Phys.* **07** (2021) 027.
- [79] CMS Collaboration, Measurement of Higgs boson production in association with a W or Z boson in the  $H \rightarrow WW$  decay channel, Technical Report No. CMS-PAS-HIG-19-017, CERN, Geneva, 2021, <https://cds.cern.ch/record/2758367>.
- [80] Albert M. Sirunyan *et al.*, Measurement of the inclusive and differential Higgs boson production cross sections in the leptonic WW decay mode at  $\sqrt{s} = 13$  TeV, *J. High Energy Phys.* **03** (2021) 003.
- [81] A. M. Sirunyan *et al.*, Observation of Higgs Boson Decay to Bottom Quarks, *Phys. Rev. Lett.* **121**, 121801 (2018).
- [82] CMS Collaboration, Measurement of Higgs boson production in the decay channel with a pair of  $\tau$  leptons, Technical Report No. CMS-PAS-HIG-19-010, CERN, Geneva, 2020, <https://cds.cern.ch/record/2725590>.
- [83] Albert M. Sirunyan *et al.*, Measurements of properties of the Higgs boson decaying into the four-lepton final state in

- pp collisions at  $\sqrt{s} = 13$  TeV, *J. High Energy Phys.* **11** (2017) 047.
- [84] Rahool Kumar Barman, Biplob Bhattacharjee, Arghya Choudhury, Debtosh Chowdhury, Jayita Lahiri, and Shamayita Ray, Current status of MSSM Higgs sector with LHC 13 TeV data, *Eur. Phys. J. Plus* **134**, 150 (2019).
- [85] Yasmine Sara Amhis *et al.*, Averages of  $b$ -hadron,  $c$ -hadron, and  $\tau$ -lepton properties as of 2018, *Eur. Phys. J. C* **81**, 226 (2021).
- [86] CMS Collaboration; LHCb Collaboration; and ATLAS Collaboration, Combination of the ATLAS, CMS and LHCb results on the  $B_{(s)}^0 \rightarrow \mu^+\mu^-$  decays, CERN Report No. CMS-PAS-BPH-20-003, LHCb-CONF-2020-002, ATLAS-CONF-2020-0492020, <http://cds.cern.ch/record/2727216>.
- [87] Roel Aaij *et al.*, Precise measurement of the  $f_s/f_d$  ratio of fragmentation fractions and of  $B_s^0$  decay branching fractions, *Phys. Rev. D* **104**, 032005 (2021).
- [88] G. Bélanger, F. Boudjema, A. Pukhov, and A. Semenov, micromegas: A program for calculating the relic density in the MSSM, *Comput. Phys. Commun.* **149**, 103 (2002).
- [89] G. Belanger, F. Boudjema, C. Hugonie, A. Pukhov, and A. Semenov, Relic density of dark matter in the NMSSM, *J. Cosmol. Astropart. Phys.* **09** (2005) 001.
- [90] Geneviève Bélanger, Fawzi Boudjema, Andreas Goudelis, Alexander Pukhov, and Bryan Zaldivar, micrOMEGAs5.0: Freeze-in, *Comput. Phys. Commun.* **231**, 173 (2018).
- [91] Ulrich Ellwanger and Cyril Hugonie, The higgsino–singlino sector of the NMSSM: Combined constraints from dark matter and the LHC, *Eur. Phys. J. C* **78**, 735 (2018).
- [92] E. Aprile *et al.*, Dark Matter Search Results from a One Ton-Year Exposure of XENON1T, *Phys. Rev. Lett.* **121**, 111302 (2018).
- [93] Yue Meng *et al.*, Dark Matter Search Results from the PandaX-4T Commissioning Run, *Phys. Rev. Lett.* **127**, 261802 (2021).
- [94] C. Amole *et al.*, Dark matter search results from the complete exposure of the PICO-60  $c_3f_8$  bubble chamber, *Phys. Rev. D* **100**, 022001 (2019).
- [95] E. Aprile *et al.*, Constraining the Spin-Dependent WIMP-Nucleon Cross Sections with XENON1T, *Phys. Rev. Lett.* **122**, 141301 (2019).
- [96] P. Cushman *et al.*, Working group report: WIMP dark matter direct detection, in *Community Summer Study 2013: Snowmass 2013 (CSS2013)*, Minneapolis, MN, United States (C13-07-29.2), [arXiv:1310.8327](https://arxiv.org/abs/1310.8327).
- [97] D. S. Akerib *et al.*, Results on the Spin-Dependent Scattering of Weakly Interacting Massive Particles on Nucleons from the Run 3 Data of the LUX Experiment, *Phys. Rev. Lett.* **116**, 161302 (2016).
- [98] Debottam Das, Ulrich Ellwanger, and Ana M. Teixeira, NMSDECAY: A fortran code for supersymmetric particle decays in the next-to-minimal supersymmetric standard model, *Comput. Phys. Commun.* **183**, 774 (2012).
- [99] W. Beenakker, R. Hopker, and M. Spira, PROSPINO: A program for the production of supersymmetric particles in next-to-leading order QCD, [arXiv:hep-ph/9611232](https://arxiv.org/abs/hep-ph/9611232).
- [100] Rojalin Padhan, Manimala Mitra, Suchita Kulkarni, and Frank F. Deppisch, Displaced fat-jets and tracks to probe boosted right-handed neutrinos in the  $U(1)_{B-L}$  model, *Eur. Phys. J. C* **82**, 858 (2022).
- [101] J. de Favereau, C. Delaere, P. Demin, A. Giammanco, V. Lemaître, A. Mertens, and M. Selvaggi, DELPHES 3, A modular framework for fast simulation of a generic collider experiment, *J. High Energy Phys.* **02** (2014) 057.
- [102] Shankha Banerjee, Biplob Bhattacharjee, Andreas Goudelis, Björn Herrmann, Dipan Sengupta, and Rhitaja Sengupta, Determining the lifetime of long-lived particles at the HL-LHC, *Eur. Phys. J. C* **81**, 172 (2021).
- [103] Serguei Chatrchyan *et al.*, Search in leptonic channels for heavy resonances decaying to long-lived neutral particles, *J. High Energy Phys.* **02** (2013) 085.
- [104] Georges Aad *et al.*, Search for displaced muonic lepton jets from light Higgs boson decay in proton-proton collisions at  $\sqrt{s} = 7$  TeV with the ATLAS detector, *Phys. Lett. B* **721**, 32 (2013).
- [105] Torbjorn Sjostrand, Stephen Mrenna, and Peter Z. Skands, PYTHIA 6.4 physics and manual, *J. High Energy Phys.* **05** (2006) 026.
- [106] Torbjorn Sjostrand, Stephen Mrenna, and Peter Z. Skands, A brief introduction to PYTHIA 8.1, *Comput. Phys. Commun.* **178**, 852 (2008).
- [107] J. Alwall, R. Frederix, S. Frixione, V. Hirschi, F. Maltoni, O. Mattelaer, H. S. Shao, T. Stelzer, P. Torrielli, and M. Zaro, The automated computation of tree-level and next-to-leading order differential cross sections, and their matching to parton shower simulations, *J. High Energy Phys.* **07** (2014) 079.
- [108] Michele Selvaggi *et al.*, Beta card for HL-LHC and HE-LHC studies, 2017, [https://github.com/delphes/delphes/blob/master/cards/delphes\\_card\\_HLLHC.tcl](https://github.com/delphes/delphes/blob/master/cards/delphes_card_HLLHC.tcl).
- [109] Michele Selvaggi, Pavel Demin, Christophe Delaere, Kevin Pedro, Joschka Lingemann, simonspa, Philip Harris, Sho Iwamoto, Geonmo Ryu, Joshua Ellis, Chase, and Adarsh Pyarelal, delphes/delphes: Delphes-3.4.2pre11, 2017.
- [110] Morad Aaboud *et al.*, Search for long-lived, massive particles in events with displaced vertices and missing transverse momentum in  $\sqrt{s} = 13$  TeV  $pp$  collisions with the ATLAS detector, *Phys. Rev. D* **97**, 052012 (2018).
- [111] Albert M. Sirunyan *et al.*, Search for long-lived particles using nonprompt jets and missing transverse momentum with proton-proton collisions at  $\sqrt{s} = 13$  TeV, *Phys. Lett. B* **797**, 134876 (2019).
- [112] Biplob Bhattacharjee, Swagata Mukherjee, Rhitaja Sengupta, and Prabhat Solanki, Triggering long-lived particles in HL-LHC and the challenges in the rst stage of the trigger system, *J. High Energy Phys.* **08** (2020) 141.
- [113] CMS Collaboration, The Phase-2 Upgrade of the CMS Level-1 Trigger, CERN Report No. CERN-LHCC-2020-004, CMS-TDR-021, 2020, <https://cds.cern.ch/record/2714892>.
- [114] Biplob Bhattacharjee, Tapasi Ghosh, Rhitaja Sengupta, and Prabhat Solanki, Dedicated triggers for displaced jets using timing information from electromagnetic calorimeter at HL-LHC, *J. High Energy Phys.* **08** (2022) 254.
- [115] Georges Aad *et al.*, Search for exotic decays of the Higgs boson into long-lived particles in  $pp$  collisions at  $\sqrt{s} = 13$  TeV using displaced vertices in the ATLAS inner detector, *J. High Energy Phys.* **11** (2021) 229.

- [116] Armen Tumasyan *et al.*, Search for long-lived particles produced in association with a Z boson in proton-proton collisions at  $\sqrt{s} = 13$  TeV, *J. High Energy Phys.* **03** (2022) 160.
- [117] A. M. Sirunyan *et al.*, Search for long-lived particles decaying to jets with displaced vertices in proton-proton collisions at  $\sqrt{s} = 13$  TeV, *Phys. Rev. D* **104**, 052011 (2021).
- [118] CMS Collaboration, The phase-2 upgrade of the CMS level-1 trigger, Technical Reports No. CERN-LHCC-2020-004, No. CMS-TDR-021, CERN, Geneva, 2020, Final version, <https://cds.cern.ch/record/2714892>.
- [119] CMS Collaboration, The phase-2 upgrade of the CMS data acquisition and high level trigger, Technical Reports No. CERN-LHCC-2021-007, No. CMS-TDR-022, CERN, Geneva, 2021, This is the final version of the document, approved by the LHCC, <https://cds.cern.ch/record/2759072>.
- [120] M. Aaboud *et al.*, Performance of the ATLAS track reconstruction algorithms in dense environments in LHC run 2, *Eur. Phys. J. C* **77**, 673 (2017).
- [121] ATLAS Collaboration, Search for long-lived, massive particles in events with displaced vertices and multiple jets in  $pp$  collisions at  $\sqrt{s} = 13$  TeV with the ATLAS detector, *J. High Energy Phys.* **06** (2023) 200.
- [122] Albert M. Sirunyan *et al.*, Search for long-lived particles using displaced jets in proton-proton collisions at  $\sqrt{s} = 13$  TeV, *Phys. Rev. D* **104**, 012015 (2021).